AN ABSTRACT OF THE THESIS OF

Jacob M. Benz for the degree of Master of Science in Nuclear Engineering presented on May 8, 2008.
Title: Calculation of Pulse Height Distributions from Deterministic Transport Simulations.

Abstract approved:

_____

Todd S. Palmer

In source-detector radiation transport simulations, pulse height distributions are a useful metric in assessing the effectiveness of nuclear instrumentation. In the area of spectroscopy, pulse height distributions are used to identify an unknown source.

It is widely believed that pulse height distributions cannot be created using deterministic methods. This quantity is routinely calculated in Monte Carlo transport codes because each history is individually tracked and the amount of energy deposited by interaction events is easily tallied.

We have developed a methodology to calculate the pulse height distribution using deterministic transport codes. The algorithm utilizes the scattered components of scalar flux which are readily calculated by iterating on the scattering source. The approach is applicable in three dimensions but we present here results from an implementation in 1D slab geometry with anisotropic scattering/angular quadrature orders up to P14/S32.

Calculation of Pulse Height Distributions from Deterministic Transport Simulations

by
Jacob M. Benz

A THESIS

submitted to

Oregon State University

in partial fulfillment of
the requirements for the
degree of

Master of Science

Presented May 8, 2008
Commencement June 2008

Master of Science thesis of Jacob M. Benz presented on May 8, 2008.

APPROVED:

_____

Major Professor, representing Nuclear Engineering

_____

Head of the Department of Nuclear Engineering and Radiation Health Physics

_____

Dean of the Graduate School

I understand that my thesis will become part of the permanent collection of Oregon State University libraries. My signature below authorizes release of my thesis to any reader upon request.

_____

Jacob M. Benz, Author

ACKNOWLEDGEMENTS

I would like to take this opportunity to thank my wife, Tammie. Without her help support, I would not be where I am today. She is both a comfort and an inspiration, and is always willing to listen to my rants. I would also like to thank my daughter, Alyson. She doesn't know it yet, but she provided many welcome and much needed distractions; keeping me sane in the process. You guys are the reason I have succeeded so far, and strive to do so in the future. Thanks and I love you both!

A big thank you also goes out to Dr. Palmer. His bug finding skills are legendary, and without them I would still be on page one. I have learned a lot from him during my time at OSU, which I hope to put to use once I am forced to get a real job.

Finally, This one's for you Mom!!! I love you and miss you.

TABLE OF CONTENTS

TABLE OF CONTENTS (Continued)

LIST OF FIGURES

1. **Introduction**

In the context of today's society, radiation detection has become more important than ever. In the wake of the terrorist attacks on September 11th 2001, and the ongoing war on terror, there is an increased urgency for the detection of radiological dispersal devices and nuclear weapons entering this country. Prior to September 11th, the urgency to examine all cargo entering the country was lacking. Much of the radiation detection instrumentation now protecting our ports of entry has been in place for only a few years and remains largely untested for the vast number of threat scenarios that exist. Additionally, there are new radiation detection methods and devices continually being proposed and researched to enhance or replace the devices presently deployed around the country. For proof-of-concept and verification of operational capabilities, the instrumentation should be subjected to a series of experiments using real threat sources and scenarios to obtain accurate experimental data. Unfortunately, due to the dangerous nature of threat sources and the prohibitive cost of implementing many of the scenarios, experimental results obtained under realistic conditions are scarce. To offset this lack of experimental data, numerical simulation is often used to design and assess radiation detection instrumentation.

1.1 Current Radiation Detection Instrumentation

Radiation detection technology generally falls into three broad categories: gas filled detectors, solid state detectors and scintillators. The most common gas-filled detector is the Geiger-Mueller (GM) counter. The GM counter operates on the premise that incident radiation will interact with and ionize the gas in the detector volume. The

GM counter operates at a very high voltage; to where the initial ion created by the incident radiation creates an avalanche of ions until no more charge can be collected and a pulse is generated. Because of this method of charge collection, GM counters can only be used to detect the presence and quantity of radiation. It is impossible for a GM counter to provide information regarding the spectrum of radiation.

Another type of gas-filled detector is a proportional counter. This uses the same mechanism as a GM counter, but it operates within a finite voltage range where the size of the generated pulse is proportional to the energy of the incident radiation. Therefore, it is possible to use these detectors for spectroscopy purposes with low energy gamma rays. Proportional counters can also differentiate between alpha and beta particles. Alpha particles deposit their entire energy over a very short range, while only a small fraction of energy from beta particles will be deposited in a typical proportional counter volume. Therefore, the pulses due to these two types of particles will be different sizes; with alpha pulses being larger than beta pulses.

Solid state (or semiconductor) detectors have many desirable aspects, especially in spectroscopy. For each interaction occurring in the detector, there are significantly more ions created than in either gas-filled detectors or scintillators. This is due to the small amount of ionization energy required to create an ion pair, a factor of 10 smaller between semiconductor and gas-filled detectors. Because of this, semiconductor detectors offer the greatest energy resolution for spectroscopic purposes. Some drawbacks include the susceptibility to damage when exposed to radiation fields, and limitations on size. In this area, there are two main types: Germanium (Ge) and Silicon (Si). Making functional solid state detectors involves creating high purity germanium

(HPGe), or silicon doped with lithium (Si(Li)). The reason for this is to create the largest possible active volume. When considering gamma spectroscopy, HPGe detectors offer the greatest energy resolution of all detectors discussed. One of the largest deficiencies in solid state detectors is the need to maintain the material at very low temperatures. These types of detectors are created by forming positive and negative regions at opposite ends of the detector material, with an "active volume" in between where incident radiation will interact. The very low temperatures are required to prevent the positive and negative ends of the material from drifting toward each other and combining; effectively neutralizing the detector volume and rendering it useless. This requirement limits the capability and size of these detectors.

Scintillators are probably the most widely used type of detector. Reasons for this include the wide variety of possible shapes, sizes, types, and low cost. Scintillators can take the forms of glass, organic liquids, and inorganic liquids. Scintillators rely on fluorescence or phosphorescence to produce light pulses that are then multiplied in a photomultiplier tube. Scintillators are most widely used in spectroscopy. The specific choice of scintillation material will depend on desired characteristics, including efficiency, light output, wavelength emission, and decay time or response time (Knoll 2000). There are various benefits and drawbacks for each type of scintillation detector, which should be carefully weighed.

1.2 Characteristics of Homeland Security Detection Problems

The types of radiation detection scenarios present in Homeland Security applications present a level of difficulty for numerical methods that are unseen in other areas of numerical simulation. A few of the scenarios of interest include radiation

detection at land border crossings, airports, and other ports-of-entry. Another growing area of interest is security of our seaports, and examining containers being unloaded from cargo ships. Each of these scenarios presents large physical dimensions that must be accurately modeled. Transporting the radiation from the source to detector over this large area in sufficient detail poses large problems for numerical methods. In many of the scenarios, as in real-world situations, the source will be well shielded. This creates deep penetration problems that are also difficult for many numerical methods. Finally, many of the scenarios will also be highly scattering. An ideal simulation tool will be one that can solve these types of problems quickly and efficiently, and remain portable enough to be used on a PC.

1.3 Scenario Analysis

The objective of scenario analysis is to determine the type of radiation present and identify potential threat sources. This requires distinguishing between a number of different source types; including naturally occurring radioactive material (NORM) like granite, threat sources including U-235 and Pu-241, nuisance sources such as the naturally occurring radioactivity in cat litter, and medical sources such as I-131 or Tc-99m. The success of scenario analysis depends on the ability to accurately predict or determine the sensitivity of the radiation detection instrumentation. One way of accomplishing this is to calculate pulse height distributions for the detection approaches being considered for a given scenario. Scenario variations may include changing the size or type of shielding, adjusting source strength, and most importantly, provide variation of source type. Additional goals of scenario analysis involve establishing an alarming metric and calculating the minimum detectable activity (MDA) for a specific detector.

The purpose of an alarming metric is to set a standard for determining when a threat source is present, as opposed to a benign or legitimate source (Smith, Gesh and Pagh 2005).

1.4 Numerical Simulation

Ideally, real measurements should be used in scenario analysis. In many situations of interest, this is not possible. Reasons include time or cost constraints, availability of sources, and safety of the public. Often, numerical simulation provides the only option for scenario analysis (Smith, Gesh and Pagh 2005).

In numerical simulation, the aim is to create a realistic scenario environment to provide a framework for accurate analysis. Each simulation should present the greatest accuracy achievable while maintaining a balance between detailed re-creation of the scenario environment, speed and efficiency. There are two primary goals of numerical methods used for scenario analysis: the first is the calculation of the radiation field produced by the source, and second is the calculation of the response of the detector to the radiation field. There are two primary classes of transport methods available to perform these calculations: deterministic and Monte Carlo. A detailed discussion of both will be given in Chapter 2.

1.5 RADSAT

The RAdiation Detection Scenario Analysis Toolbox (RADSAT) is an ongoing project funded by DOE's Nuclear Nonproliferation Division NA-22, and managed by Pacific Northwest National Laboratory (PNNL). Oregon State University's role in this project has been to research the creation of pulse height distributions from deterministic transport simulations.

The RADSAT project has two stated goals: (1) development of a efficient and accurate transport simulations; and (2) the analysis of radiation detection scenarios and the creation of a portable, integrated software package for deployment in the field. A few examples of the potential uses of RADSAT include near real-time search scenarios for training purposes, detector optimization and research, and border protection. Potential users of RADSAT include emergency or first responders, laboratory analysts, border patrol agents, and intelligence agencies (E. Smith, et al. 2005).

RADSAT utilizes a three dimensional deterministic transport code called Attila™ (Wareing 2001). Attila uses unstructured tetrahedral meshes created from computer-aided design (CAD) models that allow for very complex geometries to be easily modeled (Gesh, et al. 2005). Attila requires multi-group cross sections which are obtained from CEPXS (Coupled Electron/Photon Cross Sections) (SANL 1991). The radiation is transported from the various sources present in the problem, and the angular flux is calculated on the surface of an imaginary sphere surrounding the detector. The angular flux is then ported into MCNP5 (LANL 2005) which is used to calculate the pulse height distribution. The angular flux data from Attila is used as the boundary condition in MCNP5 for a simplified detector problem that can be quickly solved for the pulse height distribution (Gesh, et al. 2005). Porting the angular flux data into MCNP5 has created a number of problems, including formatting and accuracy issues, and the need to create a specific source definition piece of software that currently limits the ability of MCNP5 to operate in parallel, causing computational time to be greatly increased. Computational time is a large concern, and is one of the greatest weaknesses of MCNP5 in many scenarios of interest to RADSAT. Operating in parallel is an option in MCNP5 to help

improve computational efficiency by distributing a calculation across many computers at the same time. In the current evolution of RADSAT, this capability is not available, limiting the speed and efficiency of the entire package.

1.6 Detector Response Functions vs. Pulse Height Distributions

In radiation detection simulation, there are two related concepts that are of utmost importance; detector response functions (DRF) and pulse height distributions (PHD). A DRF is the real response of a detector exposed to radiation. The response can account for such processes as energy deposition, scintillation, light collection by the photomultiplier tube, the efficiency of the detector, and other effects caused by the electronics creating the pulse such as amplifier gain. A DRF will be different for each detector type, and may even differ between detectors of the same type. The pulse height distribution models the idealized energy deposition of a detector exposed to radiation. For a PHD, there are only three ways in which energy deposition events can occur: Compton scatter, photoelectric absorption, and pair production. A more detailed discussion will be provided in Chapter 3.

Both PHDs and DRFs are dependent upon a number of factors, including the various interaction cross sections of the detector material, the size and type of the detector, and the energy and type of incoming radiation (Knoll 2000). Knowledge of PHD/DRFs is important in many radiation detection and measurement applications, including Prompt Gamma Neutron Activation Analysis (PGNAA), radiotherapy dose measurement, medical imaging, and homeland security. Homeland security radiation detection applications include detection of threat sources, border security, and nonproliferation. In the cases of threat source detection and border security, PHD/DRFs are being used to

accurately interpret and analyze signals from radiation detectors to determine the type of radiation present and identify source radionuclides. Nonproliferation applications utilize PHD/DRFs in the enforcement and verification of international treaties, along with safeguarding the current stockpile of nuclear material both at home and abroad. This is accomplished by continually monitoring the energy spectrum at a specified location, including all outgoing and incoming material. In this manner, any deviation from what is expected can be seen and a more thorough investigation can take place.

1.7 Current Methods for Determining Detector Response Functions and Pulse Height Distributions

There are two methods most often employed in numerical simulation to determine detector response functions and pulse height distributions: a semi-empirical approach and Monte Carlo radiation transport simulation. In the semi-empirical case, DRFs are generated by creating an analytic model of detector response for each detector feature and, for example, using a least squares fit to combine each feature into a continuous spectrum (Gardner 2005). Because it is semi-empirical, this method employs several parameters that can be varied to fit the model to the desired result expected given a specific detector type. Another method for calculating parameters is to build up a DRF by using known sources. In each method, the detector's response can be quantified and parameters can be adjusted and applied when the source is unknown. Fixes can include adjusting the spectra to duplicate specific characteristics of NaI detectors or nonlinearity of charged particle interaction. In many simple cases, this approach can provide quick and accurate results. Complications arise for more detailed and sophisticated scenarios (Gardner and Sood 2004).

PHDs can also be generated semi-analytically. This is accomplished using the photon interaction cross section data in the solution of the Klein-Nishina equation. In addition there are a number of parameters that can be manipulated to account for the various mechanisms related to energy deposition.

The most common approach for the creation of PHDs in numerical simulation is Monte Carlo radiation transport simulation. Energy deposition is an inherently stochastic process that depends on the cross sections and geometry of the detector materials. Monte Carlo radiation transport faithfully simulates the lifecycle of radiation in the detector and naturally incorporates this stochasticity. Monte Carlo methods track every particle in a simulation from birth to death, including every interaction that occurs. This ability of Monte Carlo methods leads to a very precise model of the particle physics inside a detector volume. It is also possible to accurately model complex geometries in Monte Carlo codes such as MCNP5 (Gesh, et al. 2005). MCNP5 uses well tested and established cross section libraries. For this reason, Monte Carlo methods are considered the standard for radiation detection simulation.

In the area of radiation detection and measurement, one of the largest advantages of Monte Carlo methods is the ability to create precise and detailed pulse height distributions. It is also possible to post-process the PHDs to obtain a simplified detector response function. The most widely used example includes applying a Gaussian distribution to the PHD to broaden the peaks in an attempt to model the resolution of a specific detector type. This is called Gaussian Energy Broadening (GEB). There is much ongoing research in this area to further enhance this ability and more truthfully simulate many detector characteristics (Sood and Gardner 2004). The detector response function

depends on the detection mechanism employed by, and the design of, the specific detector used. For example, in the case of NaI detectors there is an inherent non-linearity in the energy deposition from electrons due to collisions with gamma rays. This is because the relationship varies with the energy of the incoming particle, and the scintillation efficiency of the NaI crystal (Gardner and Sood 2004). There are also inconsistencies in detector response between what should be identical detectors, because it is essentially impossible to create two identical crystals. The differences between each crystal will affect the scintillation efficiency of the detector and lead to variation in light collection. This is true even if the energy deposited into the detector is the same in each case. These characteristic variations are present in every type of detector, making accurate simulation of detector response calculations difficult.

1.8 Motivation

Numerical simulation for radiation detection of Homeland Security applications is continuing to grow in importance. Currently the only widely used method available to create a pulse height distribution is the Monte Carlo method. It is for these reasons that RADSAT ports the data from Attila into MCNP5 to create the pulse height distribution. Many of the difficulties created by porting to another code could be alleviated by having a deterministic-only option, and having all the necessary data to create a pulse height distribution in one code. In this thesis, we describe a new methodology for calculating PHDs from deterministic transport simulations. One of the goals of this research is to provide a framework and create the opportunity to have a deterministic-only option to perform the radiation transport and create a pulse height distribution. This is an area that has not been previously explored, and can create another branch of numerical simulation

that has been closed to deterministic methods; and provide another tool for users. We will evaluate the performance of our methodology relative to MCNP5 on several test problems of practical interest.

1.9 Layout of Thesis

The remainder of this thesis is organized as follows. Chapter 2 contains a more thorough description of pulse height distributions, along with the derivations of the deterministic and Monte Carlo methods used in this analysis. Chapter 3 contains a description of the detector problems used to test our methodology, and the results from the two methods with comparisons to calculations using MCNP5. Chapter 4 will present a discussion of the results and data presented in chapter 4. Chapter 5 will discuss the limitations of the research so far, as well as suggestions for further research.

2. **Methods**

In this section, we describe an approach to the calculation of a pulse height distribution in a deterministic radiation transport code. We present a derivation of the deterministic transport method discretization in slab geometry. Pulse height distributions are commonly calculated in Monte Carlo radiation transport codes, and we will use MCNP5 to generate the benchmark distributions for comparison with those from our deterministic approach.

The remainder of this chapter is organized as follows. We begin with a discussion of the challenges facing the radiation transport methods, both deterministic and Monte Carlo. We then will define the pulse height distribution and describe its behavior in several physical limits. We will end the chapter with a description of how the pulse height distribution is calculated via Monte Carlo methods, and using the data provided by our deterministic transport method.

2.1 Radiation Transport Method Challenges

The Boltzmann transport equation is an integro-differential equation that can be extremely difficult to solve in a variety of physical problems. Examples include deep penetration, heavily shielded sources, highly scattering, and physically large problems with small detector volumes (Pagh, et al. 2005). Each scenario will require accurate calculation of the radiation field and pulse height distribution.

2.1.1 Monte Carlo Radiation Transport Challenges

Monte Carlo transport includes individual history tracking resulting in direct simulation of the particle physics, geometric flexibility, and highly accurate and

straightforward calculation of the pulse height distribution (Gesh, et al. 2005). For these reasons, Monte Carlo methods, and specifically MCNP, have been a standard in the detection community for over 20 years. Many scenarios of interest to RADSAT pose difficulties for Monte Carlo methods.

Deep penetration (optically thick) problems, like those in shielding applications and nuclear well logging, are extremely difficult for standard analog Monte Carlo. To reach acceptable statistical limits many particles must be sampled because the likelihood of survivability is low. Additionally, the relationship between the size of the sampling population and the variance is not linear: there is a $\frac{1}{\sqrt{N}}$ correlation, where N is the size of the sampling population. Variance requirements for a given simulation may cause runtimes to become prohibitively long and strain the ability of the Monte Carlo method to obtain a result in a reasonable amount of time. Some Monte Carlo codes, such as MCNP5, employ variance reduction techniques (including roulette, splitting, and weight windows). The goal of variance reduction is to maximize the number of particles reaching a region of interest without biasing the end result. Variance reduction methods are the subject of much ongoing research. Viable techniques for variance reduction with PHDs currently do not exist outside of MCNPX; and this poses a dilemma for many in the detector community. [Variance reduction methods for the calculation of pulse height distributions are will not be discussed in this thesis. For a more detailed discussion of variance reduction, refer to (Brown 1996).] The types of scenarios related to Homeland Security applications, including deep penetration, highly scattering, and physically large problems with small detector volumes pose a large challenge to Monte Carlo methods;

and without variance reduction, the computational time required to sufficiently resolve these problems becomes very prohibitive.

The use of radiation detection instrumentation at our nation's borders highlights another area where the performance of Monte Carlo methods is not optimal: physically large, scattering dominated simulations. The Radiation Portal Monitor Project (RPMP) (PNNL 2008) is one of the largest ongoing projects at Pacific Northwest National Laboratory (PNNL). The goal of the RPMP is to install radiation detectors at U.S. borders, airports, and seaports and monitor all traffic entering the country. While some experimental data can be gathered, the majority of research relies on numerical simulation to provide scenario analysis. Typical problems involve modeling objects of large scale (semi-trucks and multiple lanes of traffic, shipping containers, etc) coupled with relatively small detector volumes (Pagh, et al. 2005). The physics of these scenarios requires many particles to be sampled to guarantee enough are reaching the detector volume to provide good statistics. If the source is well shielded, moving, and background radiation is included, the simulation becomes a deep penetration, time dependent problem on a large scale. To distinguish the source from the background, a very high degree of resolution is required. In realistic scenarios like this, Monte Carlo methods require many histories to be run, perhaps on the order of billions. The time and cost necessary to obtain accurate results become serious obstacles.

Another weakness in Monte Carlo methods is the lack of global solutions. Monte Carlo methods follow a particle from birth to death, and in the case of PHDs determine the energy deposition in a desired region for all particles tracked. The solution is only

available in pre-specified tally regions. In order to obtain solutions in multiple regions, more work will be required.

Finally, as with all stochastic methods, the solution has a statistical error. This error depends on geometry, size of simulation (physical and optical thickness), and number of particles sampled. In many cases of interest, the time required to obtain solutions with an acceptable statistical error may be on the order of weeks. Typical statistical error for the test problems presented in this thesis varies between 0.1% and 1%, with a maximum statistical error of approximately 10%. Results containing statistical errors of greater than 10% should not be considered valid and should be used with caution (LANL 2005).

2.1.2 Deterministic Radiation Transport Challenges

Deterministic methods provide results via solution of the linear Boltzmann transport equation. Both deterministic and Monte Carlo methods can provide the same result for a given scenario, but there are a few important differences between the methods. First, deterministic methods provide a global solution. By having a global solution, it is possible to "walk" a detector through a scenario geometry and look at specific locations of interest without the need to rerun the problem many times, assuming the detector does not interact with the radiation field. Second, in cases of interest to RADSAT, deterministic solutions are more computationally efficient than Monte Carlo methods. There are many deterministic methods that will provide accurate solutions in a very reasonable amount of time. Thirdly, there is no statistical error associated with deterministic solutions (Smith, Gesh and Pagh 2005). While there are no statistical errors

associated with deterministic methods, there are is error due to the numerical discretizations required to go from analytic to discrete equations.

It is commonly believed that it is not possible to calculate PHDs directly from the solution of a single deterministic transport problem. Monte Carlo methods, because of the simulated individual particle histories, are well-suited for the calculation of PHDs.

2.2 The Linear Characteristic (LC) Deterministic Transport Method in Slab Geometry

We have developed a slab geometry neutral particle transport code to demonstrate a new approach to the construction of the pulse height distribution from deterministic transport simulations. We will utilize the collided components of the scalar flux and the user specified multigroup cross-section data to build this distribution.

Separating the scalar flux into its collided components is illustrated in the following example. Particles that travel through the detector region without undergoing an interaction make up the uncollided or the 0^{th}-collided component of flux. The flux of particles having undergone one scattering collision in the detector is the 1^{st}-collided component of flux. By calculating the collided components of the scalar flux, information about the scattering of the particles can be preserved; most importantly, the source and final energy group of the particles as they undergo collisions in the detector. This approach for calculating source and final energy groups differs from Monte Carlo because individual histories are not simulated. The information about all the particles in the problem is kept as a function of the number of scattering events that have occurred. These data are then used to help calculate the distribution of energy deposition events, which is then mapped to the pulse height distribution. In the remainder of this section, we introduce the Boltzmann transport equation, and make the simplifications required to

obtain a slab geometry transport equation. We describe the discretizations we employ to numerically solve this equation, including a derivation of the Linear Characteristic spatial discretization, the S_N angular discretization, and the multigroup approximation in energy.

2.2.1 Boltzmann Transport Equation

Equation (2.1) below is the generalized, three dimensional, energy dependent, neutral particle Boltzmann transport equation.

$$\frac{1}{\upsilon}\frac{\partial\psi(\vec{r},E,\hat{\Omega},t)}{\partial t}+\hat{\Omega}\cdot\underline{\nabla}\psi(\vec{r},E,\hat{\Omega},t)+\sigma_t(\vec{r},E)\psi(\vec{r},E,\hat{\Omega},t) \quad = \quad \iint\sigma_s(E'\rightarrow E,\underline{\Omega}'\cdot\underline{\Omega})\psi(\vec{r},E',\hat{\Omega}',t)d\Omega'\,dE'+S(\vec{r},E,\hat{\Omega},t) \tag{2.1}$$

where υ defines the speed of the particle, $\psi(\vec{r},E,\hat{\Omega},t)$ is the angular flux (particles/cm^2-MeV-steradian-sec), $\hat{\Omega}$ represents the unit direction vector of particle travel, $\sigma_t(\vec{r},E)$ is the macroscopic total cross section (cm^{-1}), $\sigma_s(E'\rightarrow E,\underline{\Omega}'\cdot\underline{\Omega})dE'\,d\Omega'$ is the double differential scattering cross section, defining the probability per unit path length of scatter from within *dE'* about energy E' to within dE about E and within $d\Omega$*'* about Ω' to within $d\Omega$ about Ω, and $S(\vec{r},E,\hat{\Omega},t)$ represents the external source.

We now make a number of assumptions which will simplify the transport equation significantly. The first assumption is time independence. This assumption is valid due to the fact that the systems being modeled are non-multiplying and external sources and boundary conditions are also time independent. We next simplify the geometry to 1-D, azimuthally symmetric slab geometry; i.e.

$$\int_{4\pi} d\Omega \to 2\pi \int_{-1}^{1} d\mu \tag{2.2}$$

$$\psi(x,\Omega,E) \to \frac{1}{2\pi}\psi(x,\mu,E) \tag{2.3}$$

$$\underline{\Omega}\cdot\underline{\nabla}\psi(x,\mu,E) \to \mu\frac{\partial\psi(x,\mu,E)}{\partial x}, -1 \le \mu \le 1 \tag{2.4}$$

Inserting these three relations into equation 2.1 gives the slab geometry transport equation:

$$\mu\frac{\partial\psi(x,\mu,E)}{\partial x} + \sigma_t\psi(x,\mu,E) = \int dE' \int_{-1}^{1} d\mu'\sigma_s(x,\mu',E'\to E)\psi(x,\mu',E') + S(x,\mu,E) \tag{2.5}$$

Every term in equation (2.5) has been multiplied through by 2π to account for the $\frac{1}{2\pi}$ factor in equation (2.3).

If we expand the general, anisotropic scattering cross-section in terms of a series of Legendre polynomials, we obtain

$$\mu_n\frac{\partial\psi_g(x,\mu_n)}{\partial x} + \sigma_{t,g}\psi_g(x,\mu_n) = \sum_{l=0}^{L}\frac{(2l+1)}{2}\sum_{g=1}^{G}\sigma_{sl,g\to g'}(x)\phi_{l,g'}(x)P_l(\mu_n) + S_g(x,\mu_n) \tag{2.6}$$

where,

$$\phi_{l,g'}(x) = \sum_{n=1}^{N} w_n\psi_{g'}(x,\mu_n)P_l(\mu_n) \tag{2.7}$$

$$\psi_g(x,\mu_n) = \int_{E_g}^{E_{g-1}} \psi(x,\mu_n,E')dE' \tag{2.8}$$

The total group averaged cross section $\sigma_{t,g}$, and the group averaged source $S_g(x,\mu_n)$, are calculated the same way as the group averaged angular flux in equation (2.8). The group averaged scattering cross section $\sigma_{sl,g\to g'}$ represents the probability of a particle scattering from group *g* into group *g'*, for a given Legendre polynomial expansion *l*. P_l is the Legendre polynomial expansion function of order l. Additionally in equation (2.6), we have discretized the angular variable, using the S_N angular discretization with Gaussian quadrature. This involves replacing the integration over μ in equation (2.5), by a quadrature sum for a specific choice of angles and weights; dictated by *n*:

$$\int_{-1}^{1} d\mu \to \sum_{n=1}^{N} w_n \tag{2.9}$$

Therefore, equation (2.6) represents the anisotropic, slab geometry transport equation for one angle only (μ_n).

The slab geometry transport equation is well-posed if the angular flux incident on the problem boundary is specified, either as a known quantity or as some function of the exiting angular flux. Typically, transport problems in detectors are driven by particles incident on the problem boundary, and have no internal source.

2.2.2 The Linear Characteristic Spatial Discretization

Beginning with equation (2.5) written in a slightly different form:

$$\mu_n \frac{\partial \psi_n^{(j+1)}(x)}{\partial x} + \sigma_t \psi_n^{(j+1)}(x) = Q^{(j)}(x) \text{ , n = 1... N} \tag{2.10}$$

$$Q^{(j)}(x) = \frac{\sigma_s(x)}{2}\phi^{(j)}(x) + S^{(j)}(x) \quad , \tag{2.11}$$

$$\phi^{(j+1)}(x) = \sum_{i=1}^{N} w_i \psi_n^{(j+1)}(x)$$

In this equation, ψ_n is the angular flux in the n[th] angular ordinate, and ϕ is the scalar flux. Many quadrature sets are available, but Gaussian Quadrature has been used in this research.

The idea behind the Linear Characteristic spatial discretization is that it inverts the transport plus collision operator exactly, assuming that the source in each cell is spatially linear. Because the transport equation is an integro-differential equation, iteration on the scattering source is often employed to compute the solution. The LC method provides the way to calculate the angular flux using the integral transport equation:

$$\psi_n(x) = \psi_{n,inc} e^{-\sigma_{t,i}(x-x_{inc})/\mu_n} + \frac{1}{\mu_n} \int_{x_{inc}}^{x} [Q_i + Q_i^x P_{1i}(x)] e^{-\sigma_{t,i}(x-x')/\mu_n} dx' \qquad (2.12)$$

In equation 3.14:

$$Q_i = \frac{1}{2}(S_i + \sigma_{s,i}\phi_i) \qquad Q_i^x = \frac{1}{2}(S_i^x + \sigma_{s,i}\phi_i^x)$$

$$\phi_i = \sum_{m=1}^{N} w_m \psi_{m,i} \qquad \phi_i^x = \sum_{m=1}^{N} w_m \psi_{m,i}^x \qquad (2.13)$$

In these equations, the superscript "x" on the coefficients indicates the first spatial moment, or slope. The subscript "i" indicate cell averaged values. Looking at equations (2.12) and (2.13), it is apparent that if Q_i and Q_i^x are known, then the angular flux can be calculated. However, these two quantities also depend on the solution of the problem

(scalar flux). The 0th and 1st spatial moments of equation (2.10) can be used to generate equations for these quantities:

$$\frac{\mu_n}{\Delta x_i}(\psi_{n,i+1/2}-\psi_{n,i-1/2})+\sigma_{t,i}\psi_{n,i}=Q_i \tag{2.14}$$

$$\frac{3\mu_n}{\Delta x_i}(\psi_{n,i+1/2}+\psi_{n,i-1/2}-2\psi_{n,i})+\sigma_{t,i}\psi^x_{n,i}=Q^x_i \tag{2.15}$$

Solving equation (2.14) for $\psi_{n,i}$ and inserting it into equation (2.15), all the terms are known except for the exiting edge angular fluxes. These fluxes can be found by evaluating equation (2.12) on the exiting edge for a given direction:

$$\psi_{n,i+1/2}=\psi_{n,i-1/2}e^{-\sigma_{t,i}\Delta x_i/\mu_n}+\frac{Q_i}{2\sigma_{t,i}}[1-e^{-\sigma_{t,i}\Delta x_i/\mu_n}]\quad+$$
$$\frac{Q^x_i}{2\sigma_{t,i}}[(1-\frac{2}{\sigma_{t,i}\Delta x_i/\mu_n})+(1+\frac{2}{\sigma_{t,i}\Delta x_i/\mu_n}e^{-\sigma_{t,i}\Delta x_i/\mu_n})]\quad,\ \mu>0 \tag{2.16}$$

$$\psi_{n,i-1/2}=\psi_{n,i+1/2}e^{-|\sigma_{t,i}\Delta x_i/\mu_n|}+\frac{Q_i}{2\sigma_{t,i}}[1-e^{-|\sigma_{t,i}\Delta x_i/\mu_n|}]\quad+$$
$$\frac{Q^x_i}{2\sigma_{t,i}}[(1-\frac{2}{|\sigma_{t,i}\Delta x_i/\mu_n|})+(1+\frac{2}{|\sigma_{t,i}\Delta x_i/\mu_n|}e^{-|\sigma_{t,i}\Delta x_i/\mu_n|})]\quad,\ \mu<0 \tag{2.17}$$

Equations (2.16) and (2.17) make up the LC method, and allow us to solve the Boltzmann transport equation from equation (2.6) and calculate the angular flux, scalar flux, and partial currents. The LC method is very accurate. Assuming sufficient spatial resolution, the method is 4th order locally accurate. This means by reducing the width of a spatial mesh cell by 2, the spatial error will decrease in the cell by a factor of 16. If we are

considering a source-free pure absorber or a case where the source is isotropic or linearly anisotropic, the method will provide the exact solution.

2.3 Outline of Algorithm to be Employed

Because of the nature of the problem, Source Iteration will be used to step through the discretized equations and arrive at a converged scalar flux.

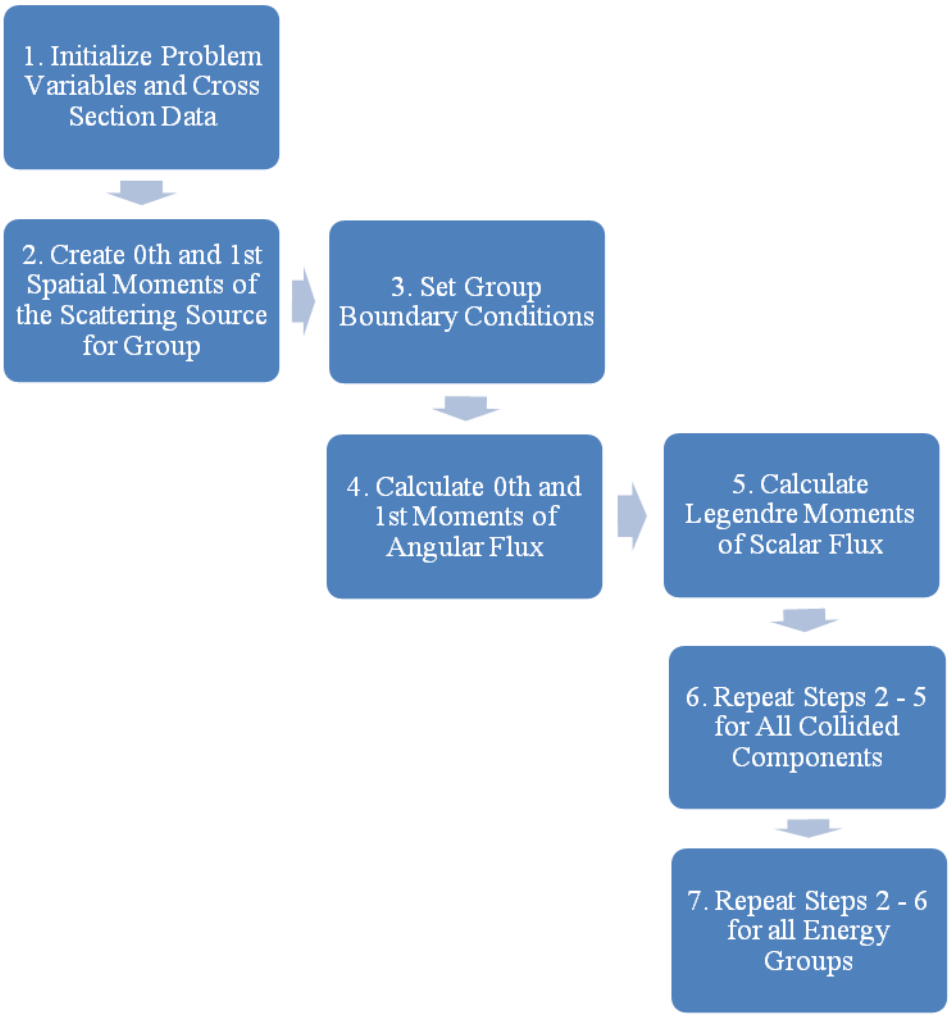

Figure 2.1: Flowchart of Algorithm Employed by LC Method

The first step is to create and initialize the required variables. These include the number and size of the cells in the problem. At this point it is also necessary to import the cross section data, number of energy groups, Gaussian quadrature angles and weights, the number of flux components to keep, and any external sources.

Source iteration requires a beginning guess for the scalar flux. One very important point here is that, in order to calculate the scattered flux components, the initial guess for the scalar flux must be zero in every cell. In addition, for the LC method the 1^{st} moment of the scalar flux must also be provided, and is also zero (since the scalar flux is constant).

First, the 0^{th} and 1^{st} moments of the scattering source are created; S and S^x. S and S^x are functions of the downscatter and inscatter reaction rates. The external source is introduced into the problem as a boundary condition. The iterations begin with the uncollided component of the first energy group, and subsequent iterations will calculate the remaining scattered components of flux for the first energy group. The number of iterations required depends only on the number of required collided components necessary to ensure convergence of the scalar flux. The external source boundary condition is set to zero while calculating the remaining components because higher scattered flux components depend only on previously calculated flux components.

Equations (2.14) and (2.15) are solved for the 0^{th} and 1^{st} spatial moments of the angular flux, from which the Legendre moments of the scalar flux are calculated and passed back to the program. The entire algorithm is repeated for the remaining energy groups.

2.4 Pulse Height Distribution

The pulse height distribution is used by the radiation detection community to identify the source of a measured radiation field. It is defined as the frequency of energy deposition events in a detector as a function of energy, caused by particles emitted by an external source. This distribution contains information about the energy spectrum of the source particles. The pulse height distribution, or $\frac{dN}{dE}$, is defined as the differential number of energy deposition events per unit energy. The total number of energy distribution events is obtained by integrating the pulse height distribution over energy. The total energy deposited in the detector can be obtained by integrating $E\frac{dN}{dE}$ over energy.

2.4.1 Small Detector Limit

There are several physical limits that give insight into the shape of the pulse height distribution. The first is the "small detector" limit, where small is defined by the mean free path of secondary gamma radiations (Knoll 2000). This definition creates detector sizes of no more than a few centimeters on average. In small detectors, the majority of incoming particles only undergo a single collision prior to leaving the detector volume (either by absorption or leakage). Therefore, two physical processes contributing to the pulse height distribution are Compton scattering and photoelectric absorption; and the result is a well defined Compton continuum and full energy peak. In the case of incoming particles with energies higher than 1.022 MeV, a double escape peak, due to pair production, will also be present.

2.4.2 Large Detector Limit

Another limit of interest is the "large detector" limit. Detectors are "large" if gamma rays, including secondary particles like scattered gamma rays and annihilation photons are all (or nearly all) absorbed in the detector volume (Knoll 2000). In this case, no incident radiation escapes the detector volume, regardless of the incoming particle energy. Therefore, despite the various interaction mechanisms acting on particles in the detector, all of the particle energy is deposited resulting in a full energy peak. In this case, the pulse height distribution would consist only of full-energy deposition events.

2.4.3 Intermediate Detector Pulse Height Distributions

In most cases, real detectors lie somewhere between these two limits. In addition to Compton continua and full energy peaks, the pulse height distribution will contain both double and single escape peaks if the incoming energy is above 1.022 MeV. Single escape peaks are caused when one annihilation photon escapes the detector and the other is absorbed in the detector. Also present will be a number of counts lying between the Compton edge and the full energy peak caused by photons undergoing multiple scattering events occurring in the detector before escaping.

2.4.4 Other Complicating Effects on the Pulse Height Distribution

Beyond the energy deposition mechanism, there are four other influences on the pulse height distribution (Knoll 2000). The first is the presence of secondary electrons. If the detector volume is small compared to the range of these electrons, a large fraction may leave the detector prior to depositing their energy. This results in a decrease in the full energy peak and may skew parts of the Compton continuum to lower energies.

Bremsstrahlung can also impact the shape of the pulse height distribution. Bremsstrahlung is caused by the slowing down of secondary particles in the detector volume. Much like the problem with secondary electrons, a significant portion of bremsstrahlung radiation may leak out of the detector prior to absorption, skewing the pulse height spectrum to lower energies.

In many cases when a photoelectric absorption occurs, a characteristic x-ray, with an energy determined by the absorber atom, is emitted. If the detector is small enough or the photoelectric absorption occurs near the surface of the detector, this x-ray may escape the detector volume. The end result is an energy deposition equal to the full energy peak minus the energy of the characteristic x-ray.

The presence of materials surrounding the detector, usually shield materials, can also influence the shape of the pulse height distribution. This occurs when particles interact in the surrounding material and deposit energy in the detector. The three main examples of this are the presence of an x-ray peak, a backscatter peak, and an annihilation peak in the pulse height spectrum. The x-ray peak is due to a photoelectric absorption in the shield and the release of a characteristic x-ray that is absorbed in the detector. A backscatter peak is caused by Compton scatter in the shield and subsequent absorption of the scattered particle in the detector. An annihilation peak, due to pair production in the surrounding material, may also be present, even if the source strength is below 1.022 MeV; cosmic radiation can interact in the shield and cause a pair production event. If one of the annihilation photons is absorbed in the detector, this event will contribute to the annihilation peak.

In the context of homeland security, the pulse height distribution is used to develop and verify detectors that form a line of defense against the possibility of nuclear attack in this country. For radiation detectors placed at border crossings, pulse height distributions are used to identify potential threats. However, the size and scope of the potential detection zone makes calculation of PHDs difficult. For example, a threat source could be transported in a tractor-trailer surrounded by a number of shielding materials that are designed to significantly depress the most recognizable radiation field. Here, the number of full energy events seen by the detector will be very few, and the Compton continuum will be inflated and perhaps skewed in energy due to the number of scattering events occurring prior to reaching the detector. Throughout, there will be varied background radiations, and possibly a variety of other sources from other vehicles contributing to the pulse height distribution. These characteristics highlight the importance of accurate calculations of the PHD.

2.5 Monte Carlo Pulse Height Distribution

Monte Carlo radiation transport codes solve the Boltzmann transport equation by faithfully simulating the life histories of radiation particles as they interact in the underlying physical medium. Pseudorandom numbers are used to sample from probability distributions describing the relevant physical interactions of radiation with matter; this approach is also called "stochastic" radiation transport. Using pseudorandom numbers and the known cross section data for the materials present in the simulation, a "random-walk" is performed and the particles are followed from birth to death, including the generation of any secondary particles. Pulse height distributions can be easily

calculated in Monte Carlo transport codes because the energy of both the initial and final energies easily determined.

At the end of each random walk, when the particle is either absorbed or leaks out of the problem, both the initial and final energy of the particle are known. Subtracting the final from the initial energy provides the total amount of energy deposited by the particle. This quantity will lie within one of the energy bins that span the range of potential energy deposition events. In whichever bin the quantity resides, a tally is added. This process is repeated until all histories have been completed. The end result is the PHD, $\frac{\Delta N}{\Delta E}$, where ΔN is the number of counts depositing energy over the small energy range ΔE. The pulse height tally is usually displayed with ΔN on the ordinate axis and the energy range on the abscissa.

2.6 Deterministic Pulse Height Distribution

Deterministic transport codes typically track energy deposition events by calculating dose rate. This quantity is fundamentally different from the pulse height energy deposition distribution. Calculations of dose rate involve the total energy deposition rate. The pulse height distribution requires information about the amount of energy deposited from each particle interaction.

As particles have interactions in the detector, it is imperative that we keep track of their initial and final energies, and we obtain this information from reaction rates using the collided components of the scalar flux. Computing the series of collided components of scalar flux requires approximately the same computational effort.

2.6.1 Energy Deposition Bin Structure

Accurate calculation of energy deposition events requires mapping from the *energy group* bin structure used in the transport calculation to the *energy deposition* bin structure for display of the pulse height distribution. The latter is completely determined by the structure of the former and is calculated in the following manner. Energy group *g* has a width defined as $\Delta E_g = E_{g,High} - E_{g,Low}$; where $E_{g,High}$ and $E_{g,Low}$ represent the high and low energy boundaries of the bin. In a downscatter event from group *g* to *g'* the corresponding range of the energy loss:

$$\Delta E_{g,g'} = \Delta E_{g,g';High} - \Delta E_{g,g';Low} \tag{2.18}$$

where,

$$\Delta E_{g,g';High} = E_{g,High} - E_{g',Low} \tag{2.19}$$

$$\Delta E_{g,g';Low} = E_{g,Low} - E_{g',High} \tag{2.20}$$

By repeatedly employing equations (3.21) and (3.22) for all values of *g* and *g'*, all possible energy losses from scattering can be precomputed. It is important to note that any particular $\Delta E_{g,g'}$ may span more than one energy deposition bin; this is most common with energy group structures that are non-uniform. Also, many group to group transfers may yield the same range of energy deposition values especially in the case of uniform energy group structures.

2.6.2 Tracking Source and Final Energy Groups

Most photon sources of interest have multiple emission lines, each of which will contribute a different full energy peak and Compton continuum in the pulse height

distribution. We have developed two important matrices that allow initial (source) and final energy groups to be computed for each group to group transfer. The first is the scattered source matrix, whose *m,g* element is calculated as:

$$\tilde{\sigma}_{s;m,g}\phi_m^{(s)} = \frac{\sigma_{s;m,g}\phi_m^{(s)}}{\sum_{g'=1}^{g}\sigma_{s;g',g}\phi_{g'}^{(s)}} \tag{2.21}$$

Equation (2.20) calculates the fractional contribution of a scattering event from group *m* to *g*, to the total scattering source in group *g*. The scattering reaction rate due to s-th collided component will come from three possible sources: external (uncollided only), downscatter, and within-group scatter.

The second matrix uses the information stored in the scattered source matrix and calculates the fraction of particles originating in source group *l*, surviving *s* collisions and arriving in group *g*. The calculation of this matrix involves a recursive formula due to the fact that, in order to survive *s* collisions and make it to group *g*, the particles must first survive $s-1$ collisions:

$$f_{l,g}^{(s)} = \sum_{m=l}^{g}\left[f_{l,g}^{s-1}(\tilde{\sigma}_{s;l,m}\phi_l^{(s-1)})\right] \quad , \tag{2.22}$$

with,

$$f_{l,g}^{(0)} = \begin{cases} 1 & \phi_l^{(0)} \neq 0 \; and \; l = g \; , \\ 0 & Otherwise \; . \end{cases} \tag{2.23}$$

2.6.3 Calculation of Energy Deposition Events

The rate of events that deposit a specified amount of energy is calculated in two pieces: those from scattering events and those from absorption events. $\Delta N_{scatter,g,g'}$ is the reaction rate of particles scattering from group *g* to group *g'*.

$$\Delta N_{scatter,g,g'} = \sum_{s} J_{g'}^{+(s)} f_{g,g'}^{(s)} \tag{2.24}$$

The outgoing partial current for the *s* collided component of flux, $J_{g'}^{+(s)}$, represents the number of particles that leave the problem in group *g'* after *s* collisions. Therefore, multiplying by $f_{g,g'}^{(s)}$ yields the number of particles in group *g'*, originating in group *g*, that have undergone *s* collisions prior to leaking out of the problem.

Finally the number of particles originating in group *g*, undergoing *s* collisions and ultimately being absorbed in group *g'*, is simply given as the absorption rate in group *g'* multiplied by $f_{g,g'}^{(s)}$:

$$\Delta N_{abs,g,g'} = \sum_{s} \sigma_{a,g'} \phi_{g'}^{(s)} f_{g,g'}^{(s)} \tag{2.25}$$

2.6.4 Construction of Pulse Height Distribution

The end result of equations (2.23) and (2.24) are two quantities, $\Delta N_{scatter,g,g'}$ and $\Delta N_{abs,g,g'}$ that include all the data necessary to construct the pulse height distribution. These quantities contain the rate at which particles that were sourced in at group *g* leak out or are absorbed in group *g'*. The next step is to map the data onto the energy deposition bin structure by stepping through every element of both matrices, equations (2.23) and (2.24), and calculating the upper and lower bounds of the energy deposition

events using equations (2.18) and (2.19). The upper and lower bounds may span one or more energy group bins, and the correct number of events must be distributed into each bin. This is accomplished by treating $\frac{dN}{dE}$ as a constant over each energy deposition range. The correct fraction is calculated by using the following equality:

$$\frac{\Delta N_x}{\Delta E_x} = \frac{\Delta N_{Total}}{\Delta E_{Total}} \tag{2.26}$$

therefore,

$$\Delta N_x = \Delta E_x \frac{\Delta N_{Total}}{\Delta E_{Total}} \tag{2.27}$$

Equation (2.26) is employed for each x, where x represents an energy bin encompassed by the total energy deposition range, ΔE_{Total}.

2.7 Summary

In this chapter, we have described a methodology for the calculation of the pulse height distribution from collided components of the scalar flux, and we have described a slab geometry deterministic transport code we will use to test the methodology. We have also presented a description of the common Monte Carlo transport approach to the calculation of the pulse height distribution.

3. **Results**

In this chapter we provide descriptions of the test problems used to evaluate the new deterministic transport method for calculating the pulse height distribution. We also investigate the importance of resolving the angular and energy discretizations for a given problem. We present the results from each test problem using our deterministic method and comparisons with the results from MCNP5.

3.1 Description of Test Problems

For our representative test problems, we have arbitrarily chosen the 1-D slab to be of length 5 cm in the x-direction, and infinite in both the y- and z-directions. Sodium Iodide (NaI) is the material making up the detector volume. For each test problem, the source will be treated as an incident boundary condition on the left face of the slab. Currently, the source is defined as incident at only one angle, but the code allows for any number of angles to be specified. Finally, in order to ensure consistency in the data, all cross sections were generated using CEPXS v1.4. The deterministic solutions use 100 equally spaced energy groups for energy discretization, in both the transport and pulse height distribution calculations; and the MCNP5 results are tallied with the same 100 energy bins. The energy group bin boundaries differ in each test problem and are dictated by the highest source energy. The energy range for test problem 1 is [0.00662 MeV, 0.6617 MeV] divided into 100 bins with constant $\Delta E = 0.00662$ MeV. Test problem 2 encompasses an energy range of [0.01334 MeV, 1.334 MeV] divided into 100 energy groups with a $\Delta E = 0.01334$ MeV. Finally the energy range of test problem 3 is [0.02615 MeV, 2.615 MeV], and 100 energy groups with $\Delta E = 0.02615$ MeV. The

deterministic transport method solution is obtained using a spatial mesh of 20 cells across the slab, and we store 20 collided components of scalar flux. Finally, in all test problems, 2.0e8 histories are used in MCNP5 to achieve reliable statistics, on the order of 0.1% to 1% statistical error.

The angular flux incident on the left face of the slab is chosen as 1e6 particles/cm^2-sec. Particles enter the left face of the slab at a grazing angle closest to normal to the left face of the detector. This angle depends on the choice of S_N order. Given the incident angular flux and the weight associated with the source grazing angle, the incoming partial current on the left face of the slab can be calculated.

The variations between each test problem are defined by the different source nuclides. The first test problem assumes a Cs-137 source. The source for the second test problem is Co-60. The last test problem uses a 1.0 μCi Th-232 source with daughter products from 100 years of ingrowth. For a detailed definition of the Th-232 source used in test problem 3, refer to Appendix A.

3.2 Test Problem 1: Cs-137 Source

Figure 3.1 shows the results from test problem 1. This graph contains the results from the deterministic PHD calculation (dN) and from MCNP5 (F8).

The deterministic pulse height distribution was created using an S_{32} angular quadrature set and P_{14} scattering order. In an S_{32} quadrature set, the source incident angle lies at $\mu_n = 0.997264$, with a corresponding weight (w_n) of 0.00701861. In general, the incident partial current on the left face of the detector is defined below in equation (2.28):

$$J^- = \sum_{\mu>0} \psi_n \mu_n w_n \tag{2.28}$$

$$J^{-} = \psi_{inc} \mu_n w_n \tag{2.29}$$

Because the source incident on the left face of the detector is monodirectional, the summation in equation (2.28) reduces to the expression in equation (2.29).

The incoming angular flux (ψ_{inc}) is 1e6 particles/cm^2-s, therefore, the incident partial current driving the source is calculated from equation (2.29) and is 6.9994e3 particles/cm^2-sec. The incident partial current is defined as the number of photons crossing the left face of the detector in the +μ direction. It is used as the particle weight (wgt) in MCNP5 to allow for a direct comparison with the deterministic transport method. In figure 3.2 we compare the scalar flux calculated from both the deterministic and MCNP5 methods, and figure 3.3 compares the exiting current on the right face of the slab from the deterministic code and MCNP5. Figures 3.2 and 3.3 provide another point of comparison between the two codes to be certain the same problem is being solved in both cases.

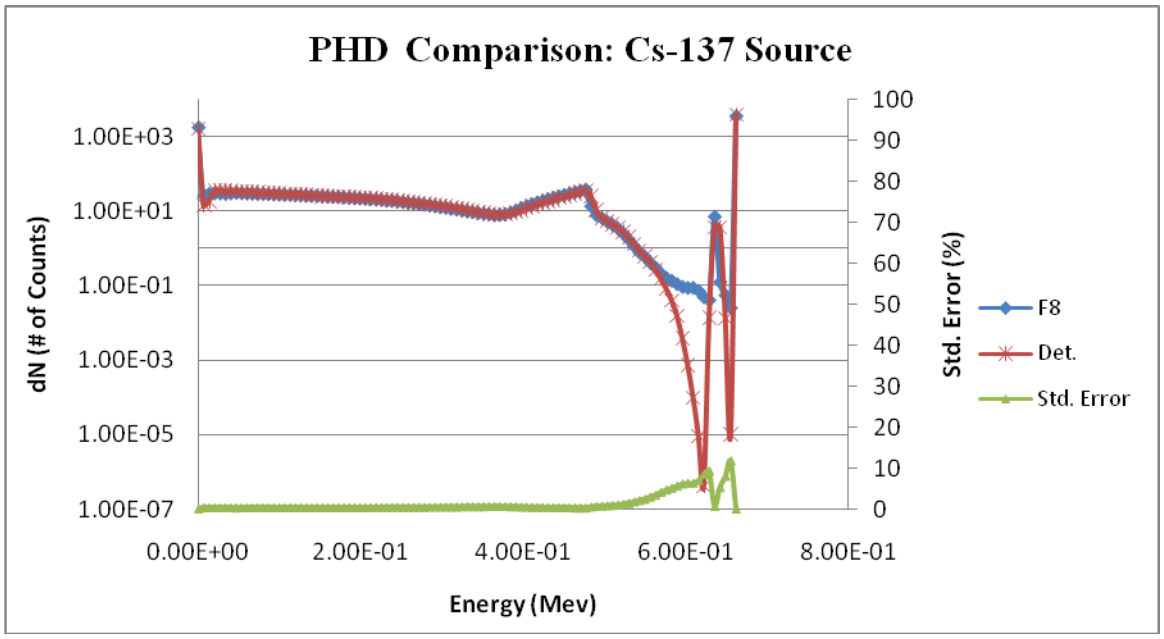

Figure 3.1: Comparison of PHD for Test Problem 1

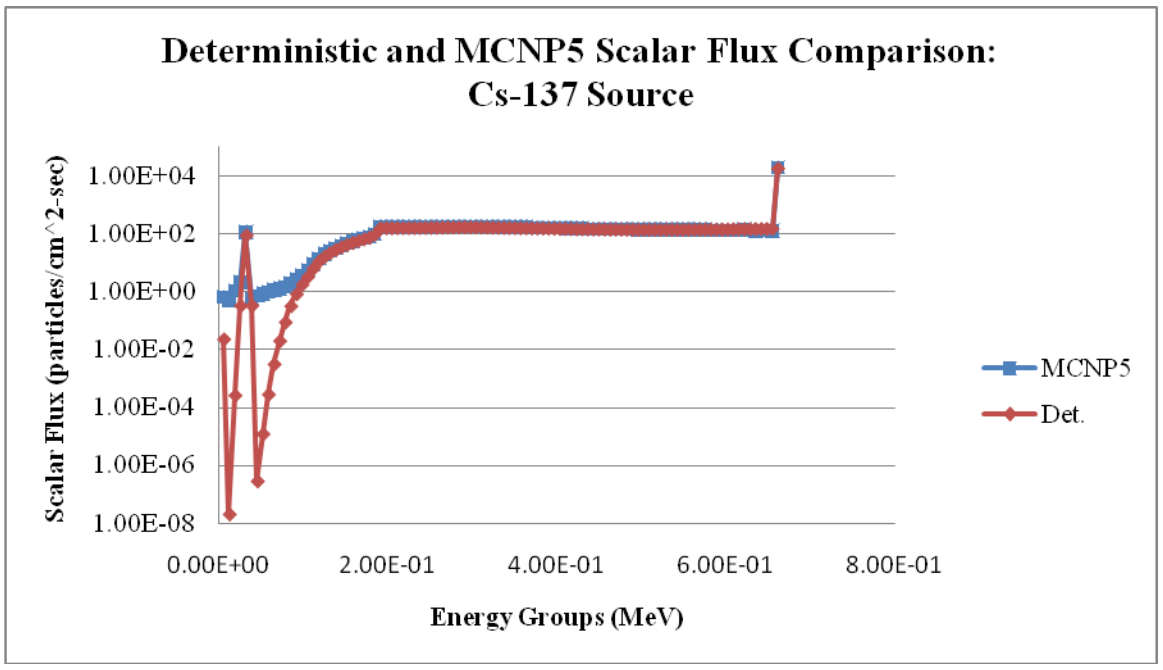

Figure 3.2: Comparison of Scalar Flux for Test Problem 1

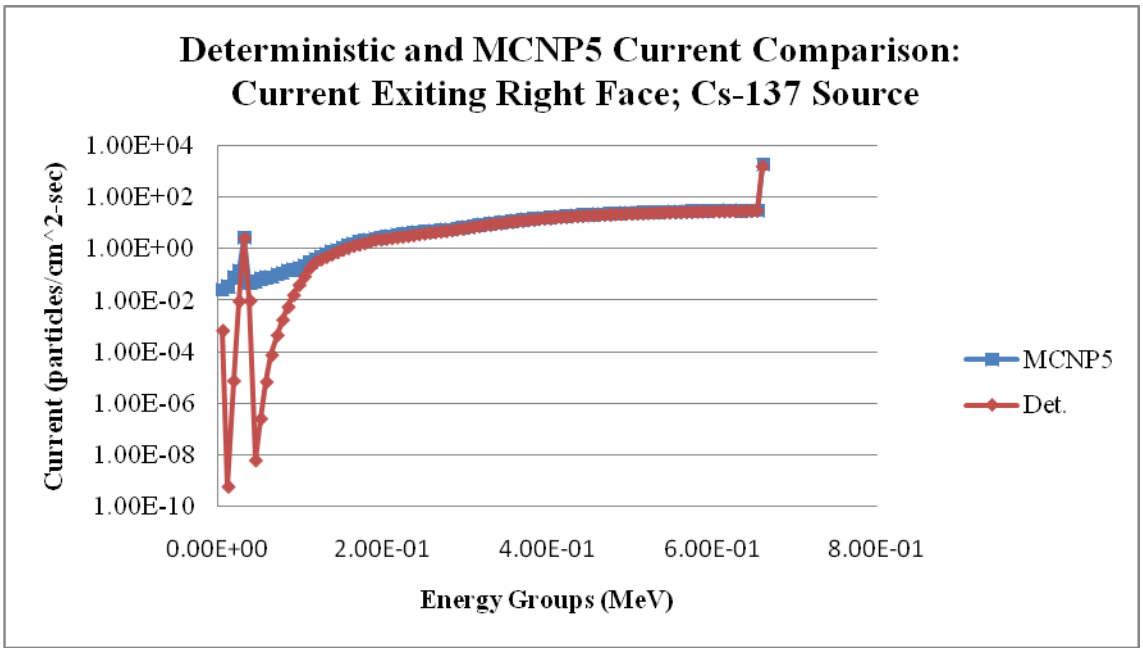

Figure 3.3: Comparison of Exiting Current on Right Face of Slab for Test Problem 1

3.3 Test Problem 2: Co-60 Source

Figure 3.4 shows the deterministic and MCNP5 pulse height distributions from a Co-60 source. The strength of the source is calculated in the same way as in test problem 1. The angular discretization is S_{32} with a P_{14} scattering order. The incident angular flux remains the same, 1e6 particles/cm^2-sec, except in this test problem, there are two source energies: 1.173 MeV and 1.332 MeV. The source strength is 1.3998e4 particles/cm^2-sec; split evenly between the two source energies. Therefore, each source energy group has an incident partial current on the left face of the detector of 6.999e3 particles/cm^2-sec; this value is used as the particle weight in MCNP5 to ensure consistency between the two transport methods. Figures 3.5 and 3.6 show deterministic and MCNP5 calculated scalar flux and partial current exiting the right face of the slab.

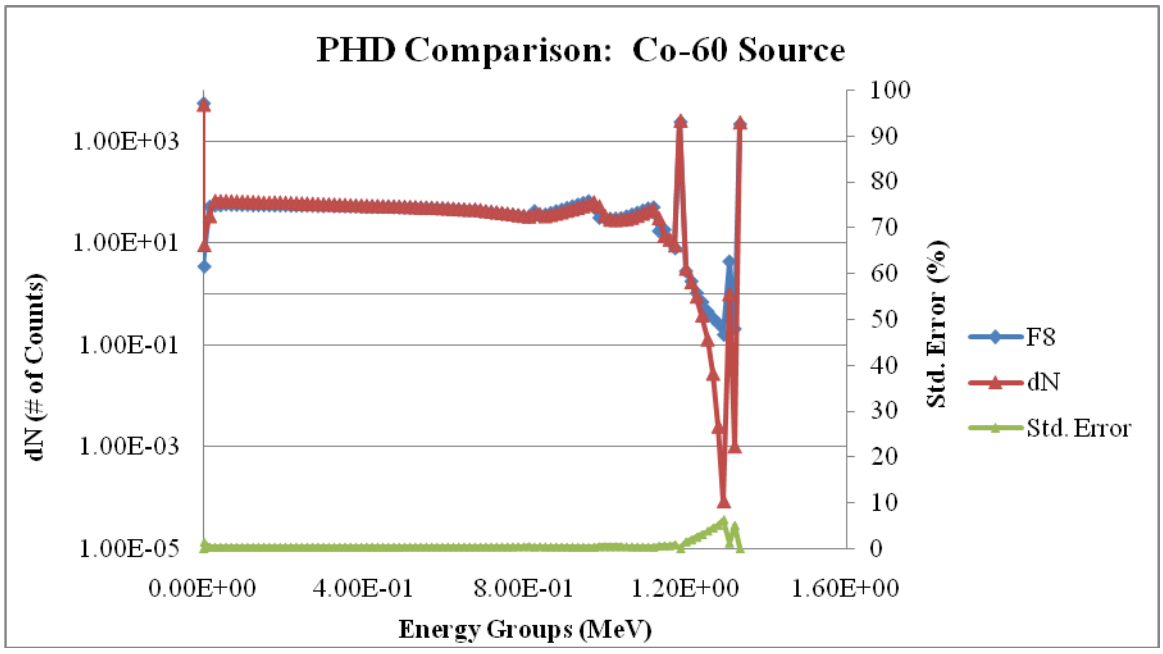

Figure 3.4: Comparison of PHD for Test Problem 2

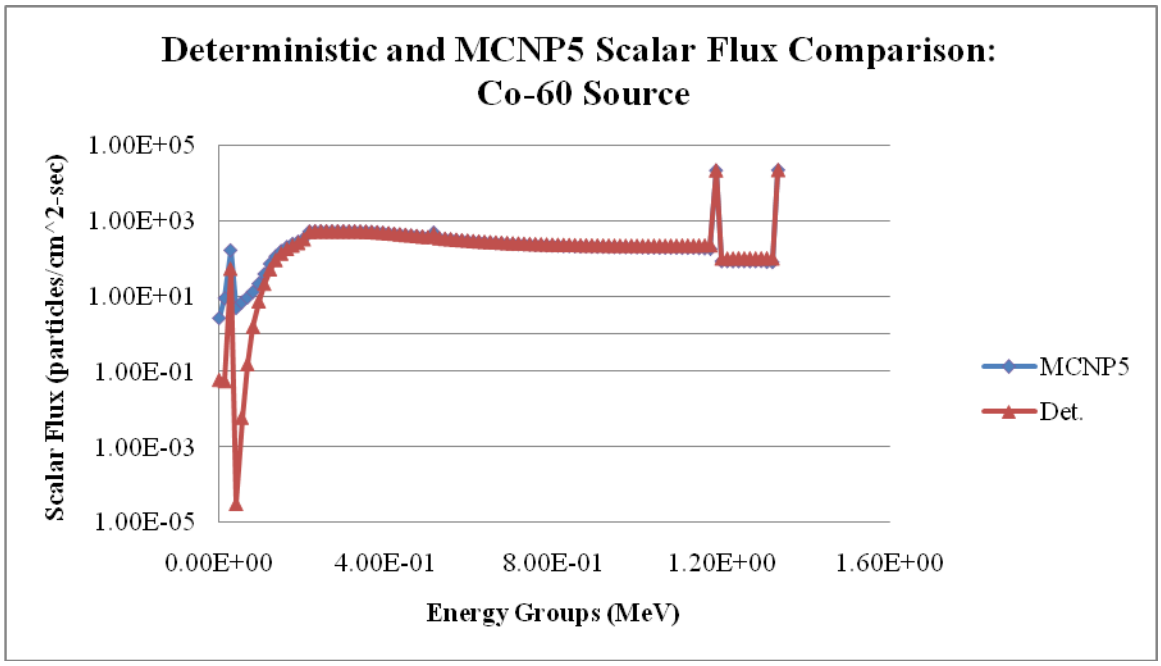

Figure 3.5: Comparison of Scalar Flux for Test Problem 2

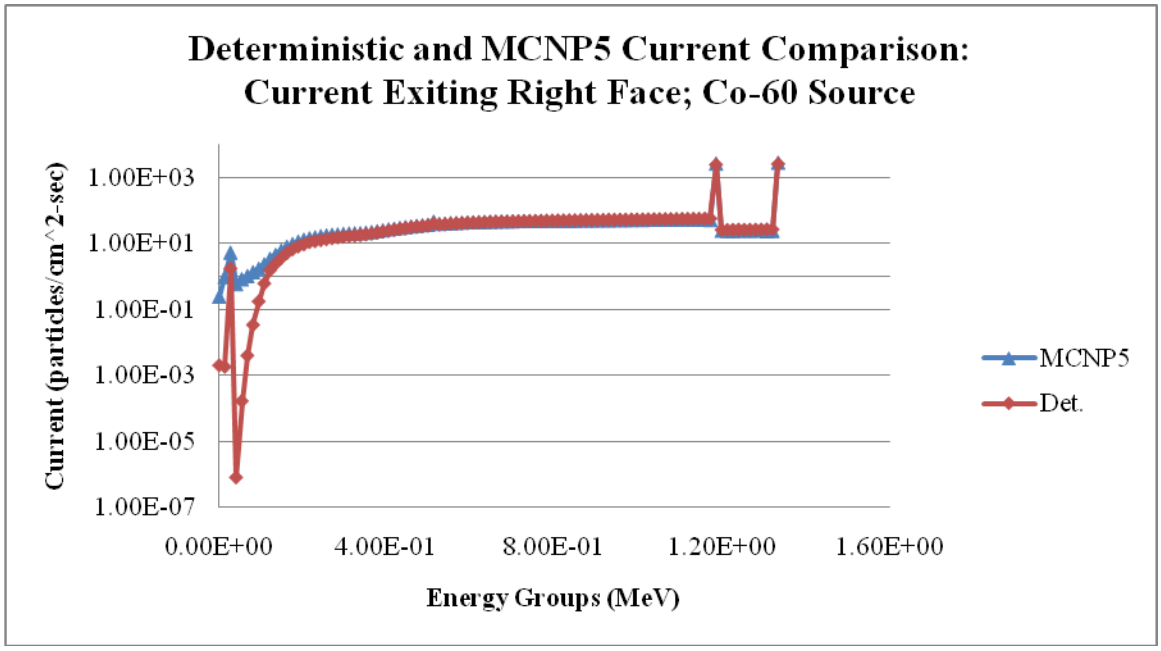

Figure 3.6: Comparison of Exiting Current on Right Face of Slab for Test Problem 2

3.4 Test Problem 3: Th-232

The strength of the Th-232 source used in this test problem is 1 µCi, with 100 years of daughter product ingrowth. There are 2.18e5 photons/sec being emitted by the source, which is the incident angular flux on the left face of the slab at an angle of μ = 0.997264, with a corresponding weight of 0.00701861. This leads to an incident partial current of 1.526e3 particles/cm^2-sec, used as the particle weight in MCNP to ensure a consistent comparison between MCNP5 and the deterministic transport method. S_{32} angular quadrature and P_{14} scattering order were used in this simulation.

A comparison of the pulse height distribution calculated using the deterministic transport method and MCNP5 are given in figure 3.7. The scalar flux from both transport approaches is displayed in figure 3.8, and the exiting partial current on the right face of the slab for both transport approaches is shown in figure 3.9.

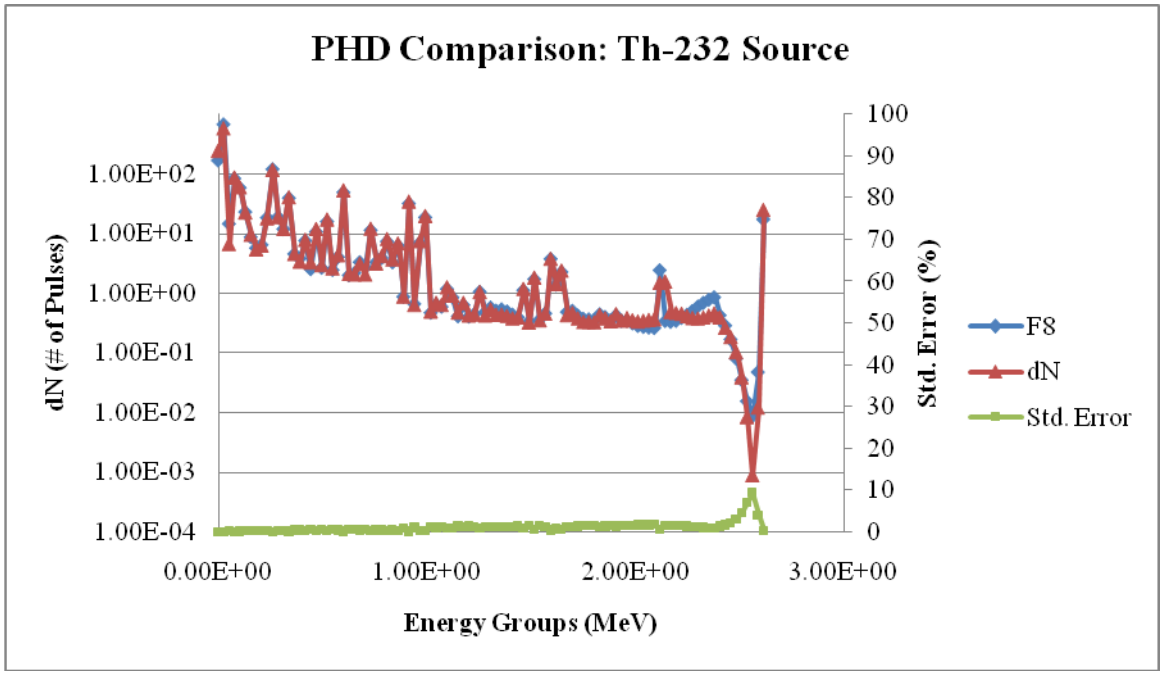

Figure 3.7: Comparison of PHD for Test Problem 3

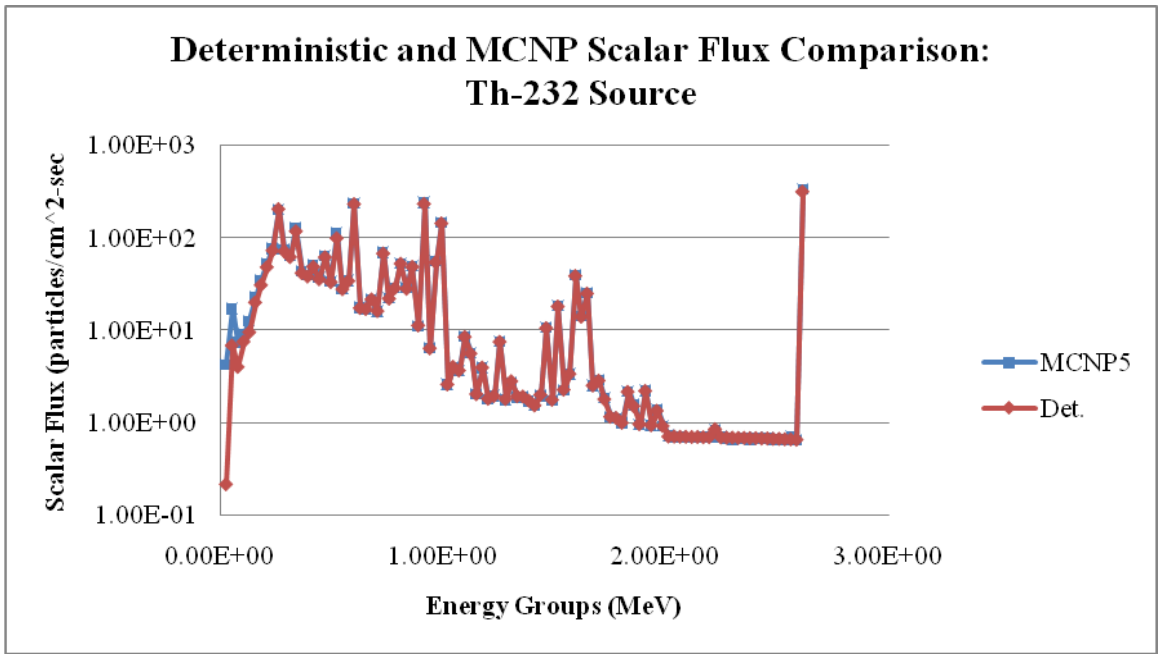

Figure 3.8: Comparison of Scalar Flux for Test Problem 3

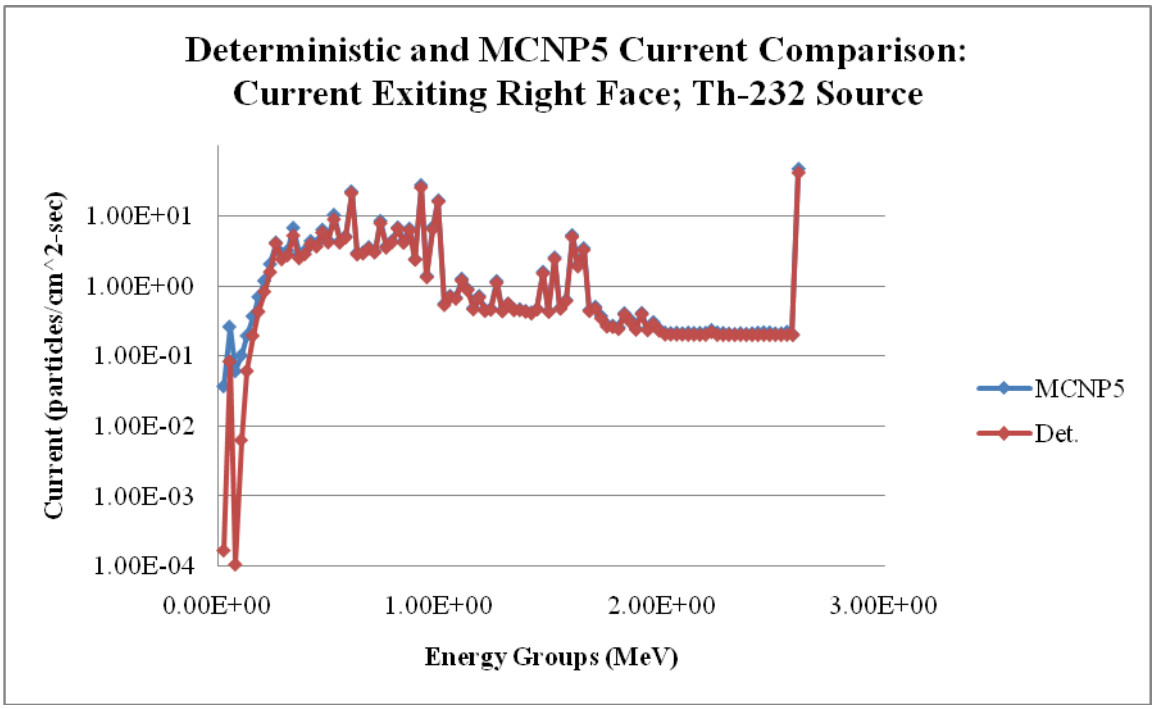

Figure 3.9: Comparison of Exiting Current on Right Face of Slab for Test Problem 3

3.5 Dependence of Quality of Deterministic Solutions on Discretization

To ensure the precision of the pulse height distribution, it is necessary to verify the convergence of the radiation transport simulation. In Monte Carlo methods, convergence can be determined in a number of ways. For example, the variance or standard deviation of the results can be a good first metric. In MCNP5, there are a number of built-in calculations that aid the user in determining convergence of the simulation. These include ten statistical checks performed and displayed in the Tally Fluctuation Chart (TFC) provided in the output file. Also provided in the MCNP5 output file is a quantity called the Figure of Merit (FOM) defined as $1/(\sigma^2 t)$, where σ is the variance and t represents the computer time in minutes (LANL 2005).

In deterministic methods, convergence depends on the choice of discretization in angle, space, time, and energy. In this research, there are two additional discretization options; scattering order, and number of collided components.

We have investigated the dependence of the deterministic transport solutions on the various discretizations by considering a simple example. We use the data from test problem 1 to run a number of simulations to show the dependence for each discretization. Figures 3.10 through 3.13 display the maximum relative error in scalar flux for each discretization as the resolution is continually refined. In order to calculate the relative error, there must be a sufficiently resolved solution to which we can compare the results. In each case the resolved solution is the solution from a "fine mesh" calculation. In figure 3.10, the spatially converged quantity is calculated on a spatial mesh with 40 cells. In figure 3.11, the relative error of the scalar flux is calculated by varying the number of angles in the angular quadrature set. The converged solution is calculated using an S_{32} angular quadrature. Figure 3.12 illustrates the maximum relative error as a function of the number of collided components of scalar flux. The converged solution is calculated using 20 collided components. Figure 3.13 displays the relative error of the scalar flux as a function of the scattering order. The converged solution is calculated using a scattering order of P_{14}.

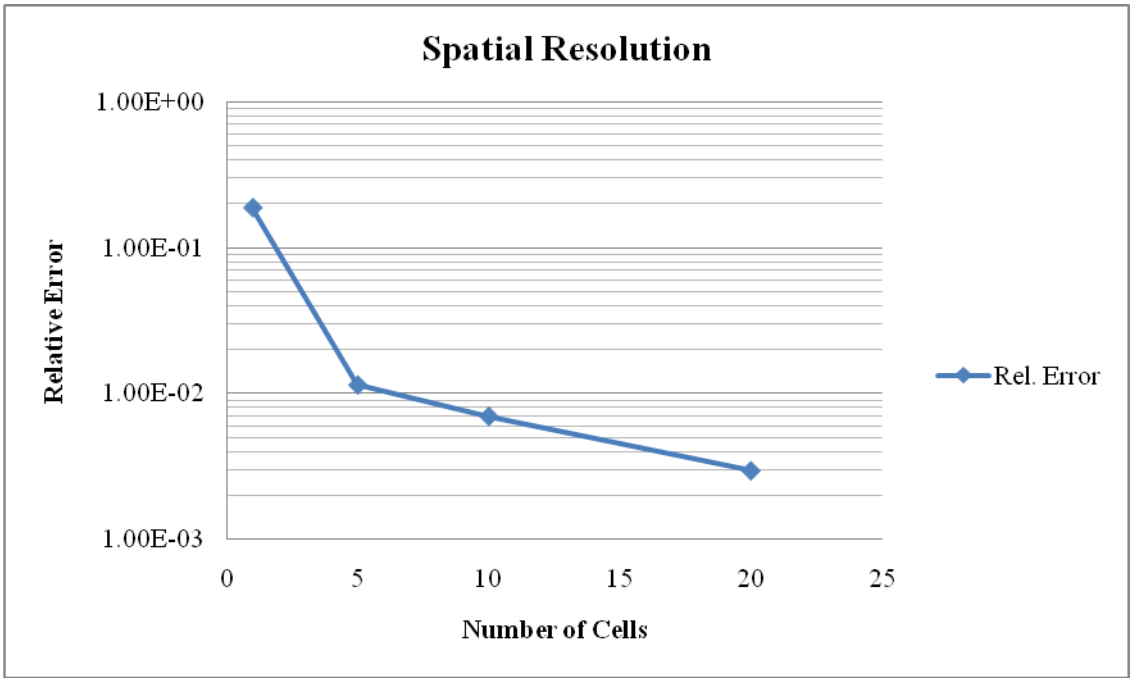

Figure 3.10: Relative Error of Scalar Flux

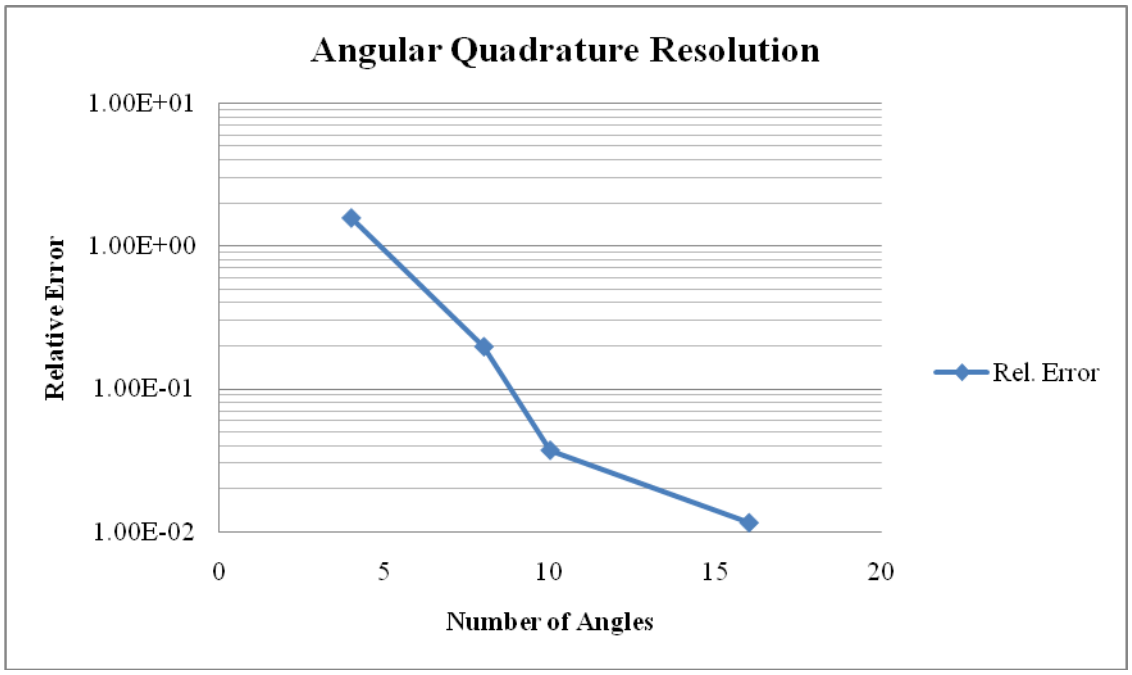

Figure 3.11: Relative Error of Scalar Flux

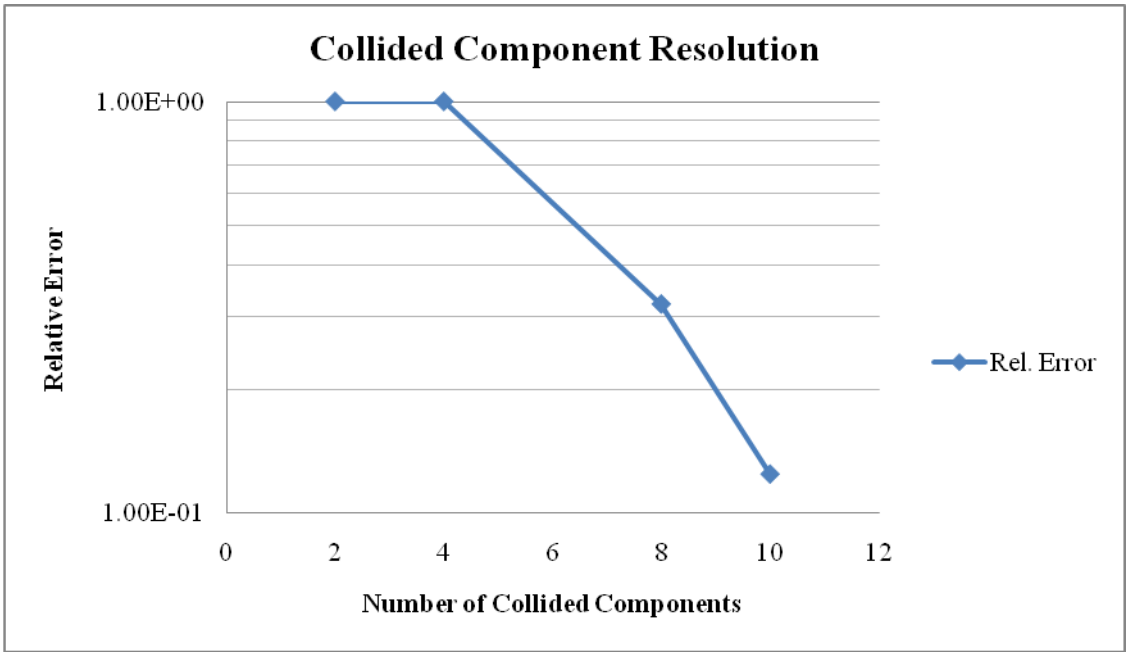

Figure 3.12: Relative Error of Scalar Flux

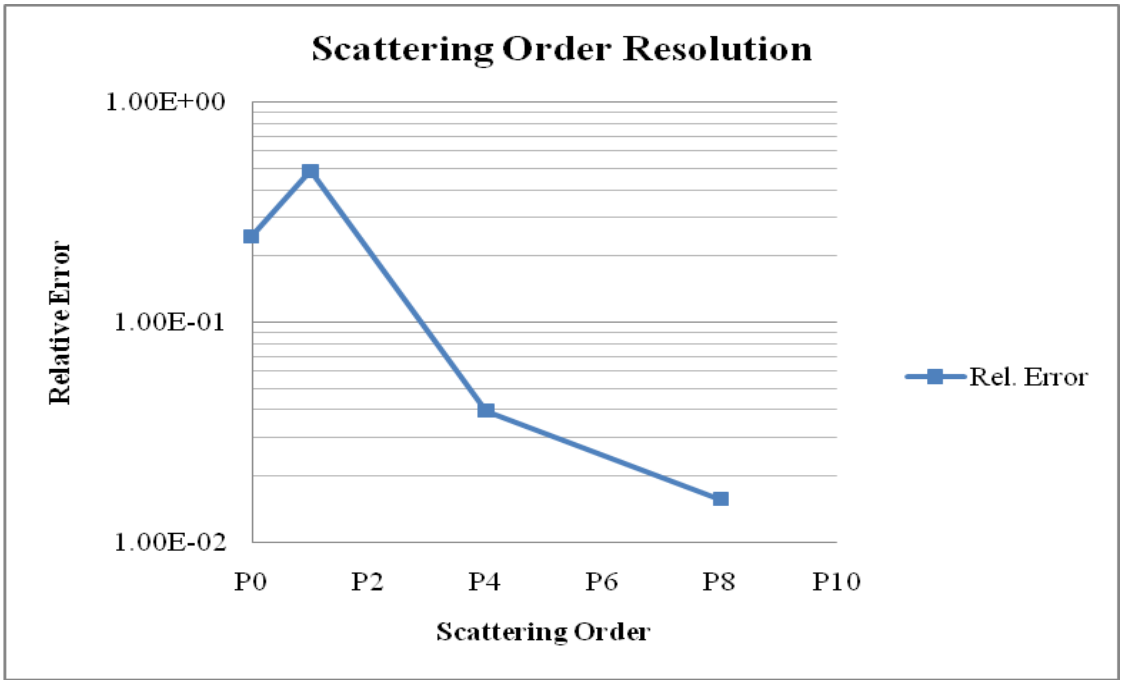

Figure 3.13: Relative Error of Scalar Flux

There is an alternative method available to aid in examining the resolution of the scattering order: we directly observe the shape of the scattering function. Each scattering function (downscatter and within group scatter) is expanded in Legendre polynomials in the scattering angle. As the order of the Legendre polynomial is increased the scattering function expansions can better handle anisotropic scattering. The scattering function expansion is defined in the following way:

$$DSF_{l,g}(\mu) = \sum_{l=0}^{N}\left[\sum_{g'=g}^{G} P_l(\mu)\sigma_{sl,g\to g'}\right] \tag{2.30}$$

$$WGSF_{l,g}(\mu) = \sum_{l=0}^{N}\left[P_l(\mu)\sigma_{sl,g\to g}\right] \tag{2.31}$$

Equation (2.27) represents the downscatter function expansion, and equation (2.28) defines the within group scattering function expansion.

As an example, we consider the same geometry and detector material as in the previous test problems, but we will only consider two energy groups. The driving source in this example is a unit incident partial current on the left face of the slab. The scattering function is most anisotropic in the fast group, and this group will be the slowest to converge. Figure 3.14 shows the shape of the within-group scattering function for P_0 through P_7 with S_{16} angular quadrature. This figure demonstrates that after P_4, there is almost no change in the angular shape of the within-group scattering function. Figure 3.15 displays the convergence of the downscatter function for P_0 through P_7 with S_{16}. The downscatter function is more anisotropic than the within-group scattering function. From these plots, we see that the convergence of the within-group and downscatter

function requires at least a scattering order of P_8. This agrees very well with the conclusions drawn using the first method described above. As the number of energy groups is increased, the within group scattering function will be more anisotropic, since only "glancing" events will allow the particle to remain in the group after a scatter event. This may become important in certain transport simulations. Additionally, it is important to vary the S_N order in an attempt to minimize the scattering function expansion and reduce the runtime for a given simulation.

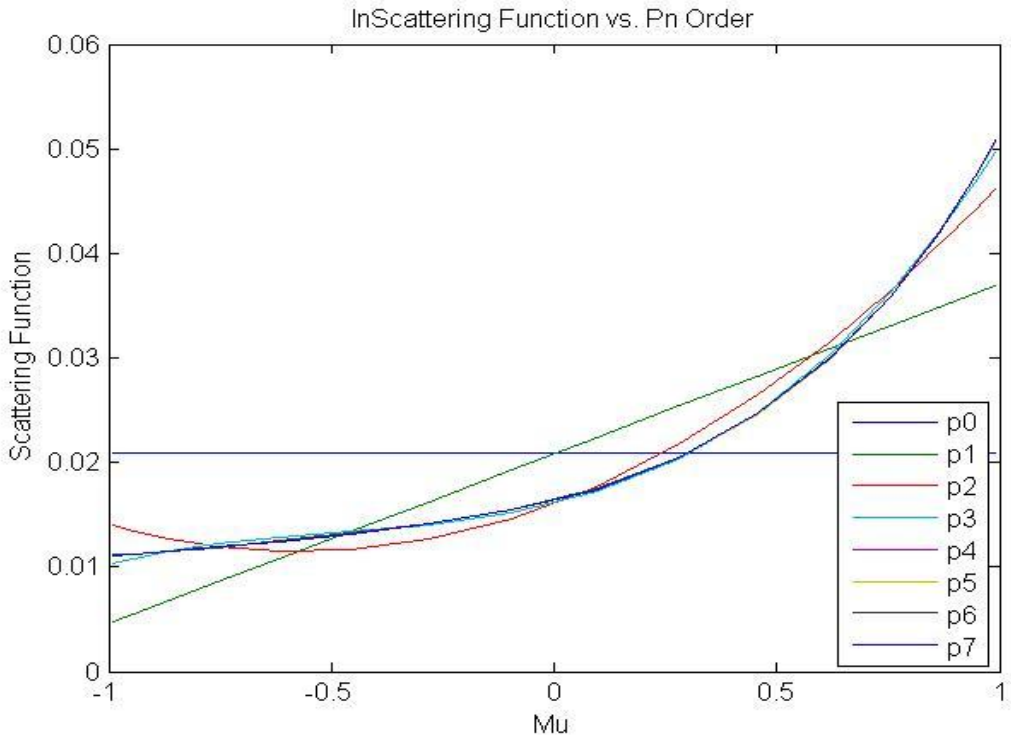

Figure 3.14: Within Group Scattering Function vs. Pn Order (P0 – P7)

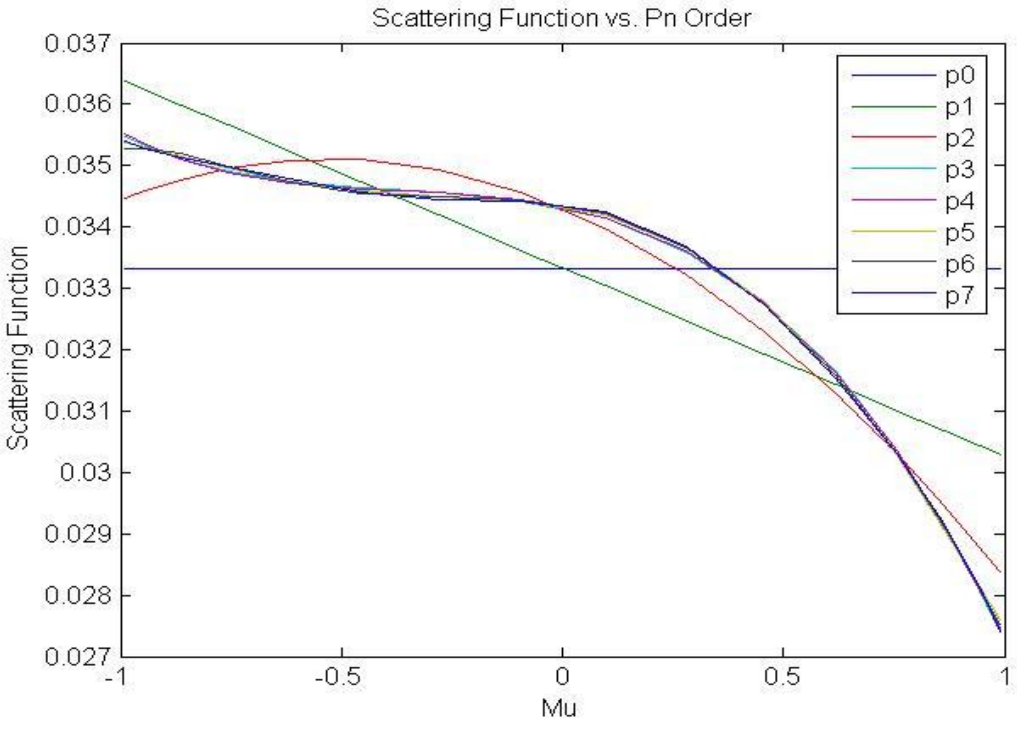

Figure 3.15: Downscatter Function vs. Pn Order (P0 – P7)

4. **Discussion**

This chapter contains a discussion of the results of the test problems presented in the previous chapter. In the initial sections, we will comment on the outcomes from the three test problems. We then offer discuss the resolution criteria required to obtain precise data from the deterministic transport method.

4.1 Test Problem 1: Cs-137

Results from test problem 1 were calculated using high resolution in all independent variables: 20 spatial cells across the slab, S_{32} angular quadrature, P_{14} scattering order, and 20 collided components of the scalar flux. Figure 3.1 shows that there is excellent agreement in each of the three peaks of the pulse height distribution: the full energy peak located in the energy group bin containing 0.6617 MeV, the x-ray escape peak located in the energy group bin holding 0.635 MeV, and the peak in the lowest energy group bin at 1.0e-5 MeV. The characteristic (k-shell) x-ray emitted by NaI has an energy of 28 keV. The x-ray escape peak located in the bin surrounding 0.635 MeV corresponds to a full energy deposition of 0.662 MeV minus the characteristic x-ray energy of 0.028 MeV.

There is a small discrepancy between the MCNP5 and deterministic x-ray escape peaks in figure 4.1. This is due to the energy resolution of the test problem. The value of the x-ray escape peak lies very near the boundary between the 0.635 MeV and 0.642 MeV energy bins. Because of the fine energy resolution desired, the counts belonging to the x-ray escape peak are distributed between these two bins in the deterministic pulse height distribution calculation. If the boundaries of the energy group structure are shifted, the counts making up the x-ray escape peak will be properly distributed in one

bin. This is a consequence of the use of multigroup cross section data in the transport calculation and is an important consideration in the choice of energy group structure.

The peak in the lowest energy bin (1.0e-5) is an artificial peak generated by MCNP5. It contains the number of particles that have streamed through the slab uncollided. In this way MCNP5 can ensure particle conservation. For consistency, we have included the uncollided (0^{th} collided) component of the partial current exiting the right face of the slab, and locate the results in the same lowest energy bin. The two methods generate very comparable results in this lowest energy bin.

There is also excellent agreement throughout the entire Compton continuum, and Compton edge. Looking at the similarities between the peaks and Compton continuum and edge, we can conclude that, using MCNP5 as our correct solution, we are correctly calculating the amount of energy deposited in the slab from both photoelectric absorption and Compton scatter in this simple test problem.

The most significant deviations between the methods are in the region between the Compton edge and x-ray escape peak, and between the x-ray escape peak and full energy peak. These regions are often called multiple scatter regions. One possible reason for this difference is the cross section data being used by the two codes. MCNP5 utilizes continuous energy cross section data while CEPXS generates multigroup cross section data. The downscatter cross section from CEPXS is zero in this energy range until after the 4^{th} scattering event. The magnitude of the component of flux with 4 or more scatters is insignificant compared to the first three collided components. The scattering reaction rates after the 4^{th} collided component result in very few energy deposition events that which is evident in the deterministic pulse height distribution in

figure 3.1. It is possible that the continuous energy data in MCNP5 will generate a small number of low probability downscatter events in this energy range after one or two scattering events. Figure 3.1 shows that the number of pulses calculated by MCNP5 in this energy range is greater than that while calculated from the deterministic method.

Figures 3.2 and 3.3 compare the average scalar flux and exiting partial currents from the two transport methods. There is excellent agreement in nearly all regions of importance; photoelectric absorption depositing energy over the range [0.65508 MeV, 0.662MeV], x-rays located in the energy group bounded by the range [0.019851 MeV, 0.026468 MeV], and also the Compton continuum. The most significant discrepancy between the two approaches is in the multiple scatter region. These figures suggest that the fundamental difference between the two methods is in the particle transport – if the fluxes and exiting partial currents agreed in the multiple scatter region, it is likely the PHD would agree as well.

In each of the important energy ranges, the full energy peak, x-ray escape peak, and Compton continuum, the results from the deterministic transport code are indistinguishable from those calculated using MCNP5. In the energy ranges where discrepancy exists, the cause is likely differences in nuclear data between the two codes.

4.2 Test Problem 2: Co-60

The same problem specifications used in test problem 1 are used here: 20 spatial cells, S_{32} angular quadrature, P_{14} scattering order, and 20 collided components of flux. Figure 3.4 provides a comparison of the pulse height distribution calculated using MCNP5 and our deterministic transport method. At each of the two full energy peaks (1.17 MeV and 1.33 MeV) depositing energy in the groups bounded by [1.159 MeV,

1.1725 MeV] and [1.3205 MeV, 1.334 MeV] respectively, and at the peak located in the lowest energy group (described previously), there is excellent agreement between the two methods. Although the two source energies are emitted with the same probability, there is an unequal probability of absorption. There is a higher likelihood of absorption for the 1.17 MeV source gammas because the absorption cross section is larger at lower energies. Normally, the sizes of the two peaks differ by roughly 10%. Figure 3.4 appears to display peaks of equal size. Looking at the data, the peak value for 1.17 MeV gammas is 2.57e3 counts, while the peak value for 1.33 MeV gammas is 2.37e3 counts. The difference between the peak values is 0.2 MeV. The 1.33 MeV peak is roughly 10% smaller than the 1.17 MeV peak; which is what should be expected. The logarithmic scale of figure 3.4 makes this difference difficult to observe graphically. There is a single escape peak, caused by pair production occurring from the 1.33 MeV gammas, which is present in this test problem that was not in test problem 1. This is because each of the source energies lies above the pair production threshold of 1.022 MeV. The Compton continuum and Compton edges are nearly identical in the two methods.

There are two regions in this plot where the methods do not agree as well: the multiple scatter region and the x-ray escape peak. The multiple scatter region was discussed in test problem 1. The x-ray peak value calculated from our deterministic transport method is 0.994 while the value calculated using MCNP5 is 4.33. The end result is the deterministic calculation being a factor of 4.35 lower. We suspect this difference is caused by differences in the scattering cross section between CEPXS and MCNP5.

Figures 3.4 and 3.5 show the average scalar fluxes and exiting partial currents for the two methods. Overall, there is good agreement between the codes, with differences again in the multiple scatter region and at the x-ray escape peak.

4.3 Test Problem 3: Th-232

This last test problem involves a source for which there are 362 discrete source energies and associated probabilities of emission. Figure 3.7 compares the pulse height distributions calculated from MCNP5 and our deterministic transport method. At each of the peak energies, the magnitudes of the coincident peaks are virtually indistinguishable from each other. An important difference occurs in the peak located in the energy bin containing 2.12 MeV. This peak corresponds to the single escape peak from pair production events caused by the 2.62 MeV photons in the highest energy bin. The peak, as calculated by our deterministic transport method is spread over two energy bins, just like the x-ray escape peak in test problem 1. This is a consequence of the choice of energy bin boundaries, and can be alleviated by a different choice of boundaries. The sum of the counts in each of the two energy bins is equal to the number of counts in the single escape peak calculated by MCNP5.

Also, throughout the majority of the Compton continuum, the results calculated from each method are the same. However, the portion of the Compton continuum and edge that lie above the single escape peak differ between the methods. Our deterministic transport method is unable to accurately match the slope over this range. Lastly, the same discrepancy in the multiple scatter region is present in this test, although the difference is significantly smaller than in the previous two test problems.

In figures 3.8 and 3.9, the scalar fluxes and exiting currents on the right face of the slab from MCNP5 and the deterministic method are shown respectively. One noteworthy difference occurs at 0.0523 MeV. MCNP5 calculates a scalar flux of 17.3 photons/cm^2-sec and a partial current of 2.61e-1 photons/cm^2-sec in this energy bin. Our deterministic transport method gives values of 6.9 photons/cm^2-sec and 8.36e-2 photons/cm^2-sec for scalar flux and exiting partial current respectively. This peak corresponds to the x-ray escape peak due to photoelectric absorption occurring in the 2.615 MeV source energy group. Looking at the pulse height distribution in figure 3.7, the x-ray escape peak is indistinguishable from the Compton continuum.

4.4 Quality of Discretizations on Deterministic Solutions

In the previous chapter we described the spatial, angular, scattering order, and collided component discretizations used in out deterministic code. In this section, we investigate the dependence of the quality of our results on the resolution in each of these variables. We have chosen the Cs-137 test problem, test problem 1, as the basis for comparison. We have examined the angular dependence of the scattering function to determine the scattering order necessary for accurate results.

4.4.1 Spatial Resolution

Figure 3.10 shows the relative difference in scalar flux between coarse spatial meshes and a "converged" fine mesh result calculated using 40 equal sized cells across the slab. Spatial discretizations of 1, 5, and 10 cells results in a maximum relative error of greater than 10%. A spatial discretization of 20 cells results in a maximum relative error of less than 1%. There is no analytic result with which to compare our numerical

results, but these test problems do show a reduction in error as the mesh is refined. Figure 3.10 indicates that a minimum of 10 cells should be used to obtain reasonable accuracy.

4.4.2 Angular Resolution

Figure 3.11 shows the maximum relative error of the scalar flux as a function of the number of angles in the quadrature set. The "converged" solution is calculated using S_{32} angular quadrature. This figure suggests that quadratures smaller than S_{16} yield unacceptably large errors in the solution. In more complicated geometries, highly scattering problems or scenarios where ray effects are present, substantially more angular resolution may be required.

4.4.3 Collided Flux Component Resolution

Figure 3.12 shows the maximum relative error in scalar flux as a function of the number of collided flux components used in the simulation. The "converged" result is calculated using 20 collided flux components. The number of collided components being used by the simulation is similar to replacing the number of iterations on the scattering source in normal source iteration. If an insufficient number of collided components are not kept, we may not be iterating to convergence on the scalar flux. Figure 3.12 shows that keeping only 2 or 4 collided components yields very inaccurate results. With 8 collided components, the maximum relative error is still large at 34%, and keeping 10 collided components gives an error of 12%. In this test problem, a minimum of 10 collided components is necessary to obtain reasonably accurate results.

4.4.4 Scattering Order Resolution

Figure 3.13 shows the maximum relative error in the scalar flux calculated as a function of the order of the scattering function expansion. The "converged" solution is calculated using P_{14} scattering, which means a 14^{th} order Legendre polynomial expansion is used. The scattering order is a measure of the amount of anisotropy of the scattering cross section. For example, if the scattering function is isotropic or linearly anisotropic, then a polynomial expansion of order 0 or 1 (P_0 or $P_{1)}$ will exactly characterize the scattering function. The more anisotropic the scattering, the higher the scattering order must be to accurately represent the scattering function. In the Cs-137 example problem, we show that P_0 and P_1 are insufficient to accurately represent the scattering function. P_4 gives a maximum relative error of 3.95% and a scattering order of 8 results in a maximum relative error of 1.57%. In this test problem, the scattering function can be represented by a polynomial of order 3 with a relative error of less than 4%.

An alternative approach involves looking directly at the scattering function. Figure 3.14 shows the within group scattering function as a function of P_N order. This figure also shows that a scattering order of P_4 is sufficient to accurately recreate the within group scattering function curve. Figure 3.15 displays the results for the downscatter scattering function. A visual inspection of this figure indicates that P_5 scattering is enough to accurately reproduce the anisotropy of the downscatter scattering function.

4.4.5 Resolution of Energy Group Structure

The quality of the numerical solution generated by the deterministic transport code is dependent on the number of energy groups used to generate the cross section data. Most often, energy resolution (group structure) is problem dependent and specified at the outset. However, in some radiation detection problems, the choice of group structure is dictated by the energy resolution available in instrumentation or from measurements.

5. **Conclusions**

In this section, we discuss the limitations of the research presented in this thesis, and discuss future work necessary to completely validate the research and methods we have presented.

5.1 Limitations

We have demonstrated a new method for deterministic calculation of the pulse height distribution in 1D slab geometry. In principle, however, the extension to three dimensions is straightforward. The physics of the algorithm we have developed requires only that the scalar flux be generated from post-processing, and 3-D deterministic transport codes are available that can perform these calculations in complex geometries.

Some of the discrepancies exhibited in our test problems may be due to differences in the cross section data. To verify whether or not this is the case may require exploration into alternative cross section data than that provided in CEPXS.

Another current limitation of this research is that we have assumed that the radiation field is known on the face of the detector. However, it is not a difficult process to move the source away from the slab. There are two ways we could approach a solution. First we could run deterministic transport using normal source iteration, for example, and calculate the angular flux at the face of the detector from a shielded source located an appreciable distance away. At this point we would run another deterministic simulation this angular flux as our boundary condition, and run in collided component mode (using the method

presented in this thesis). The other option would be to run the entire problem using collided components. The only difficulty here is the number of components necessary to accurately represent scattering over the entire problem.

5.2 Future Work

To fully reproduce the capabilities of MCNP5, pair production must be better treated in the deterministic calculation of PHDs. In some cases, coupled photon/electron transport may be necessary to generate very accurate PHDs. Coupled deterministic electron/photon transport is possible in 1-D (through CEPXS-ONELD) and 3-D (through Attila). Coupled electron/photon transport may improve the energy deposition events near the surface of a detector where some of the electron energy can escape.

This research has presented a limited number of test problems. Further research will involve a larger number of detector geometries (in multiple dimensions), and also detector materials. Another area of research may involve post-processing PHDs to mimic simplified detector response functions. MCNP5 accomplishes this with Gaussian Energy Broadening (GEB) functions to account for resolution issues of detectors.

5.3 Summary

We have described a new approach to the calculation of the pulse height distribution in radiation detectors. Our methodology is the first to use deterministic transport instead of Monte Carlo transport. This methodology has been tested using a 1-D slab geometry linear characteristic transport code, and for several test problems, its results (scalar flux, exiting partial current, and pulse height distribution) compare very favorably with MCNP5.

References

Adams, M.L., and E.W. Larsen. "Fast Iterative Methods for Discrete Ordinates Particle Transport Calculations." *Progress in Nuclear Energy, Volume 40, Number 1*, 2002: 2-159.

Brown, F.B. and Sutton, T.M. *Monte Carlo Fundamentals.* KAPL-4823 (DOE/TIC-4500-R75), Schenectady: KAPL, 1996.

Gardner, Robin P. "Detector Response Function Status and Need." *Transactions of the American Nuclear Society.* American Nuclear Society, 2005. 423-424; Volume 93.

Gardner, Robin P., and Avneet Sood. "A Monte Carlo Simulation Approach for Generating NaI Detector Response Functions (DRFs) That Accounts for Non-linearity and Variable Flat Continua." *Nuclear Instruments and Methods in Physics Research B 213*, 2004: 87-99.

Gesh, C.J., G.H. Meriwether, R.T. Pagh, and L.E. Smith. "Coupled Deterministic/Monte Carlo Simulation of Radiation Transport and Detector Response." *Transactions of the American Nuclear Society.* American Nuclear Society, 2005. 419-422, Volume 93.

Knoll, Glenn F. *Radiation Detection and Measurement.* John Wiley & Sons, 2000.

LANL. *MCNP — A General Monte Carlo N-Particle Transport Code, Version 5: User's Manual.* LA-CP-03-0245, Los Alamos National Laboratory, 2005.

LANL, Los Alamos National Laboratory. "MCNP - A General Monte Carlo N-Particle Transport Code, version 5." LA-UR-03-1987, 2003.

Pagh, R.T., R.T. Kouzes, R.J. McConn, S.M. Robinson, J.E. Schweppe, and E.R. Siciliano. "Computer Modeling of Radiation Portal Monitors for Homeland Security Applications." *Transactions of the American Nuclear Society.* American Nucler Society, 2005. 415-418, Volume 93.

PNNL. *National Security Directorate: Radiation Detection and Nuclear Sciences.* February 2008. http://rdnsgroup.pnl.gov/projects.stm#rpm (accessed May 2008).

SANL, Sandia National Laboratory. "CEPXS v.1.17, A Multigroup Coupled Electron-Photon Cross Section Generating Code." SAND91-1806, 1991.

Smith, Eric L., Christopher Gesh, and Richard Pagh. "Transport Method Challenges in Radiation Detection Scenario Analysis." *Transactions of the American Nuclear Society.* American Nuclear Society, 2005. 413-414, Volume 93.

Smith, Eric, Christopher Gesh, Richard Pagh, Walt Hensley, and Ken Jarman. *Lifecycle Plan Concept Paper,FY06.* Internal, Pacific Northwest National Laboratory, 2005.

Sood, Avneet, and Robin P. Gardner. "A New Monte Carlo Assisted Approach to Detector Response Functions." *Nuclear Instruments and Methods Physics Research B 213*, 2004: 100-104.

Sood, Avneet, R. Arthur Forster, Bryce J. Adams, and Morgan C. White. "Verification of the Pulse Height Tally in MCNP5." *Nuclear Instruments and Methods in Physics Research B 213*, 2004: 167-171.

Wareing, T.A., McGhee, J.M., Morel, J.E., Pautz, S.D. "Discontinuous finite element SN methods on three-dimensional unstructured grids." *Nuclear Science and Engineering, Vol. 138, No. 3*, 2001: 256-268.

APPENDIX

Appendix A: Source Definition file for Th-232 with 100 years of ingrowth

Source Energy (MeV)	Prob. Of Emission	Photons/sec	Nuclide		ZAID	Num. Density
0.0089534	2.54E-04	5.55E+01	Bi	212	830212	3.63E+03
0.0091845	3.98E-05	8.69E+00	Tl	208	810208	1.83E+02
0.0094195	5.69E-04	1.24E+02	Pb	212	820212	3.83E+04
0.009658	3.63E-06	7.93E-01	Bi	212	830212	3.63E+03
0.010137	1.23E-05	2.68E+00	Ra	224	880224	3.16E+05
0.0102585	5.15E-03	1.12E+03	Bi	212	830212	3.63E+03
0.0105409	7.91E-04	1.73E+02	Tl	208	810208	1.83E+02
0.010622	3.00E-04	6.55E+01	Th	228	900228	6.04E+07
0.0108281	1.11E-02	2.43E+03	Pb	212	820212	3.83E+04
0.0109938	4.80E-05	1.05E+01	Bi	212	830212	3.63E+03
0.011118	1.50E-03	3.28E+02	Ac	228	890228	2.21E+04
0.0111185	6.97E-05	1.52E+01	Bi	212	830212	3.63E+03
0.0113493	1.06E-05	2.32E+00	Tl	208	810208	1.83E+02
0.011712	1.47E-04	3.21E+01	Pb	212	820212	3.83E+04
0.0117131	2.27E-04	4.96E+01	Ra	224	880224	3.16E+05
0.012085	1.06E-06	2.31E-01	Bi	212	830212	3.63E+03
0.0122816	5.98E-03	1.31E+03	Bi	212	830212	3.63E+03
0.0123246	5.31E-03	1.16E+03	Th	228	900228	6.04E+07
0.0127014	7.40E-04	1.62E+02	Tl	208	810208	1.83E+02
0.01276	3.22E-02	7.03E+03	Ra	228	880228	1.81E+08
0.012855	5.69E-06	1.24E+00	Ra	224	880224	3.16E+05
0.012952	2.56E-02	5.59E+03	Ac	228	890228	2.21E+04
0.0130993	1.02E-02	2.24E+03	Pb	212	820212	3.83E+04
0.0135009	6.88E-05	1.50E+01	Bi	212	830212	3.63E+03
0.01352	1.69E-01	3.70E+04	Ra	228	880228	1.81E+08
0.013662	1.60E-04	3.49E+01	Th	228	900228	6.04E+07
0.0143363	3.09E-04	6.75E+01	Ra	224	880224	3.16E+05
0.014511	6.64E-04	1.45E+02	Ac	228	890228	2.21E+04
0.0145628	1.38E-03	3.02E+02	Bi	212	830212	3.63E+03
0.0148839	1.37E-04	2.98E+01	Tl	208	810208	1.83E+02
0.01515	1.69E-02	3.70E+03	Ra	228	880228	1.81E+08
0.0152303	8.01E-03	1.75E+03	Th	228	900228	6.04E+07
0.0153763	1.92E-03	4.20E+02	Pb	212	820212	3.83E+04
0.0158689	1.34E-05	2.92E+00	Bi	212	830212	3.63E+03
0.016154	3.47E-02	7.57E+03	Ac	228	890228	2.21E+04
0.01618	7.62E-02	1.67E+04	Ra	228	880228	1.81E+08

0.0168813	6.68E-05	1.46E+01	Ra	224	880224	3.16E+05
0.0179517	1.80E-03	3.94E+02	Th	228	900228	6.04E+07
0.0188	2.20E-02	4.81E+03	Ra	228	880228	1.81E+08
0.0191132	7.85E-03	1.71E+03	Ac	228	890228	2.21E+04
0.0194	1.52E-03	3.33E+02	Ra	228	880228	1.81E+08
0.0398458	1.86E-03	4.07E+02	Bi	212	830212	3.63E+03
0.0578137	8.89E-04	1.94E+02	Ac	228	890228	2.21E+04
0.0589921	3.22E-04	7.03E+01	Th	232	900232	4.43E+17
0.0708316	1.27E-04	2.77E+01	Bi	212	830212	3.63E+03
0.0728035	1.30E-03	2.84E+02	Tl	208	810208	1.83E+02
0.0728729	2.14E-04	4.68E+01	Bi	212	830212	3.63E+03
0.0748137	1.79E-02	3.90E+03	Pb	212	820212	3.83E+04
0.0749693	2.19E-03	4.78E+02	Tl	208	810208	1.83E+02
0.0768582	1.01E-04	2.21E+01	Bi	212	830212	3.63E+03
0.0771073	3.00E-02	6.56E+03	Pb	212	820212	3.83E+04
0.07929	1.69E-04	3.68E+01	Bi	212	830212	3.63E+03
0.0810674	2.09E-04	4.56E+01	Ra	224	880224	3.16E+05
0.0824337	7.56E-05	1.65E+01	Bi	212	830212	3.63E+03
0.083787	3.46E-04	7.56E+01	Ra	224	880224	3.16E+05
0.084257	2.05E-03	4.48E+02	Th	228	900228	6.04E+07
0.0847893	7.73E-04	1.69E+02	Tl	208	810208	1.83E+02
0.0851851	2.12E-05	4.64E+00	Bi	212	830212	3.63E+03
0.0854291	2.97E-05	6.49E+00	Th	228	900228	6.04E+07
0.0871902	1.06E-02	2.32E+03	Pb	212	820212	3.83E+04
0.0876316	2.23E-04	4.88E+01	Tl	208	810208	1.83E+02
0.088471	4.88E-05	1.07E+01	Th	228	900228	6.04E+07
0.0896389	5.98E-05	1.31E+01	Bi	212	830212	3.63E+03
0.0899547	5.80E-03	1.27E+03	Ac	228	890228	2.21E+04
0.0901281	3.15E-03	6.89E+02	Pb	212	820212	3.83E+04
0.0926726	1.82E-05	3.98E+00	Bi	212	830212	3.63E+03
0.09335	9.42E-03	2.06E+03	Ac	228	890228	2.21E+04
0.0946774	1.22E-04	2.67E+01	Ra	224	880224	3.16E+05
0.0979075	3.90E-05	8.53E+00	Ra	224	880224	3.16E+05
0.0995475	2.27E-03	4.96E+02	Ac	228	890228	2.21E+04
0.0999155	1.75E-05	3.82E+00	Th	228	900228	6.04E+07
0.1033407	5.70E-06	1.24E+00	Th	228	900228	6.04E+07
0.1053616	3.41E-03	7.45E+02	Ac	228	890228	2.21E+04
0.1089898	1.13E-03	2.47E+02	Ac	228	890228	2.21E+04
0.1151221	1.00E-03	2.19E+02	Pb	212	820212	3.83E+04
0.1240876	2.74E-05	5.98E+00	Bi	212	830212	3.63E+03
0.1243673	7.28E-05	1.59E+01	Th	232	900232	4.43E+17
0.1290348	4.96E-03	1.08E+03	Ac	228	890228	2.21E+04
0.1300666	3.04E-05	6.65E+00	Bi	212	830212	3.63E+03

0.1314968	2.16E-04	4.72E+01	Th	228	900228	6.04E+07
0.1314968	7.71E-09	1.68E-03	Fr	224	870224	1.60E+02
0.1356828	2.95E-05	6.44E+00	Ac	228	890228	2.21E+04
0.1411871	8.35E-05	1.82E+01	Ac	228	890228	2.21E+04
0.1439876	1.70E-05	3.72E+00	Bi	212	830212	3.63E+03
0.1460594	4.84E-04	1.06E+02	Ac	228	890228	2.21E+04
0.15389	1.43E-03	3.12E+02	Ac	228	890228	2.21E+04
0.1639876	7.91E-06	1.73E+00	Bi	212	830212	3.63E+03
0.1641456	7.75E-06	1.69E+00	Pb	212	820212	3.83E+04
0.1664293	2.33E-10	5.09E-05	Fr	224	870224	1.60E+02
0.1664293	1.39E-04	3.03E+01	Th	228	900228	6.04E+07
0.1741802	5.40E-05	1.18E+01	Ac	228	890228	2.21E+04
0.1765774	8.65E-05	1.89E+01	Pb	212	820212	3.83E+04
0.1847173	2.32E-04	5.06E+01	Ac	228	890228	2.21E+04
0.1900666	4.26E-05	9.31E+00	Bi	212	830212	3.63E+03
0.1912894	2.06E-04	4.51E+01	Ac	228	890228	2.21E+04
0.1995398	4.68E-04	1.02E+02	Ac	228	890228	2.21E+04
0.2043677	2.67E-04	5.83E+01	Ac	228	890228	2.21E+04
0.2057452	4.82E-05	1.05E+01	Th	228	900228	6.04E+07
0.2057452	1.28E-09	2.79E-04	Fr	224	870224	1.60E+02
0.2093852	6.98E-03	1.52E+03	Ac	228	890228	2.21E+04
0.2107595	3.93E-04	8.58E+01	Ac	228	890228	2.21E+04
0.2113055	1.03E-04	2.26E+01	Tl	208	810208	1.83E+02
0.2157538	4.69E-04	1.02E+02	Th	228	900228	6.04E+07
0.2157538	1.67E-08	3.65E-03	Fr	224	870224	1.60E+02
0.2162404	1.33E-03	2.91E+02	Ac	228	890228	2.21E+04
0.2204883	2.33E-05	5.09E+00	Ac	228	890228	2.21E+04
0.2237161	1.12E-04	2.46E+01	Ac	228	890228	2.21E+04
0.2323474	9.82E-05	2.15E+01	Ac	228	890228	2.21E+04
0.2333229	1.88E-04	4.11E+01	Tl	208	810208	1.83E+02
0.2385784	7.39E-02	1.62E+04	Pb	212	820212	3.83E+04
0.2407643	6.61E-03	1.44E+03	Ra	224	880224	3.16E+05
0.2524527	4.86E-04	1.06E+02	Tl	208	810208	1.83E+02
0.2572874	5.40E-05	1.18E+01	Ac	228	890228	2.21E+04
0.2635654	9.82E-05	2.15E+01	Ac	228	890228	2.21E+04
0.2702561	6.39E-03	1.39E+03	Ac	228	890228	2.21E+04
0.277283	4.13E-03	9.02E+02	Tl	208	810208	1.83E+02
0.2792584	3.93E-04	8.58E+01	Ac	228	890228	2.21E+04
0.2820244	1.50E-04	3.28E+01	Ac	228	890228	2.21E+04
0.288084	5.78E-04	1.26E+02	Bi	212	830212	3.63E+03
0.2904808	1.52E-05	3.33E+00	Ra	224	880224	3.16E+05
0.2950876	4.08E-05	8.91E+00	Bi	212	830212	3.63E+03
0.3000336	5.66E-03	1.24E+03	Pb	212	820212	3.83E+04

0.321912	4.27E-04	9.34E+01	Ac	228	890228	2.21E+04
0.3252026	4.19E-10	9.16E-05	Fr	224	870224	1.60E+02
0.3276742	2.28E-04	4.97E+01	Ac	228	890228	2.21E+04
0.3278235	3.26E-10	7.12E-05	Fr	224	870224	1.60E+02
0.3279297	2.31E-04	5.05E+01	Bi	212	830212	3.63E+03
0.3280698	5.86E-03	1.28E+03	Ac	228	890228	2.21E+04
0.3324763	8.01E-04	1.75E+02	Ac	228	890228	2.21E+04
0.3349107	5.12E-10	1.12E-04	Fr	224	870224	1.60E+02
0.3384199	2.11E-02	4.60E+03	Ac	228	890228	2.21E+04
0.3409398	8.87E-04	1.94E+02	Ac	228	890228	2.21E+04
0.3568347	3.34E-05	7.30E+00	Ac	228	890228	2.21E+04
0.3722728	1.47E-05	3.22E+00	Ac	228	890228	2.21E+04
0.3779352	5.40E-05	1.18E+01	Ac	228	890228	2.21E+04
0.3831426	2.98E-10	6.51E-05	Fr	224	870224	1.60E+02
0.3888728	2.46E-05	5.37E+00	Ac	228	890228	2.21E+04
0.3968728	5.50E-05	1.20E+01	Ac	228	890228	2.21E+04
0.3992365	6.19E-05	1.35E+01	Ac	228	890228	2.21E+04
0.4092903	6.78E-06	1.48E+00	Ra	224	880224	3.16E+05
0.4096246	3.73E-03	8.14E+02	Ac	228	890228	2.21E+04
0.4143684	4.10E-10	8.95E-05	Fr	224	870224	1.60E+02
0.4151556	4.77E-05	1.04E+01	Pb	212	820212	3.83E+04
0.4161728	2.95E-05	6.44E+00	Ac	228	890228	2.21E+04
0.4172529	5.59E-11	1.22E-05	Fr	224	870224	1.60E+02
0.4192252	4.42E-05	9.66E+00	Ac	228	890228	2.21E+04
0.4335128	2.44E-05	5.32E+00	Bi	212	830212	3.63E+03
0.4404871	2.46E-04	5.37E+01	Ac	228	890228	2.21E+04
0.4495689	1.10E-04	2.40E+01	Ac	228	890228	2.21E+04
0.4527734	6.15E-04	1.34E+02	Bi	212	830212	3.63E+03
0.4608419	8.99E-05	1.96E+01	Ac	228	890228	2.21E+04
0.4631049	7.73E-03	1.69E+03	Ac	228	890228	2.21E+04
0.4713728	5.89E-05	1.29E+01	Ac	228	890228	2.21E+04
0.4733586	8.52E-05	1.86E+01	Bi	212	830212	3.63E+03
0.4743246	4.91E-05	1.07E+01	Ac	228	890228	2.21E+04
0.4781974	4.08E-04	8.91E+01	Ac	228	890228	2.21E+04
0.481792	1.47E-05	3.21E+00	Ac	228	890228	2.21E+04
0.4857752	3.04E-05	6.64E+00	Tl	208	810208	1.83E+02
0.4923558	3.44E-05	7.51E+00	Ac	228	890228	2.21E+04
0.4926191	1.03E-05	2.26E+00	Bi	212	830212	3.63E+03
0.4982645	7.34E-05	1.60E+01	Ac	228	890228	2.21E+04
0.5037075	3.64E-04	7.94E+01	Ac	228	890228	2.21E+04
0.5091719	8.35E-04	1.82E+02	Ac	228	890228	2.21E+04
0.5106055	1.31E-02	2.87E+03	Tl	208	810208	1.83E+02
0.5152396	7.37E-05	1.61E+01	Ac	228	890228	2.21E+04

0.5199744	1.33E-04	2.90E+01	Ac	228	890228	2.21E+04
0.5231832	2.06E-04	4.51E+01	Ac	228	890228	2.21E+04
0.5404728	4.91E-05	1.07E+01	Ac	228	890228	2.21E+04
0.546361	3.73E-04	8.15E+01	Ac	228	890228	2.21E+04
0.549704	1.19E-04	2.59E+01	Rn	220	860220	5.56E+01
0.5552728	8.35E-05	1.82E+01	Ac	228	890228	2.21E+04
0.5626522	1.71E-03	3.74E+02	Ac	228	890228	2.21E+04
0.570232	3.14E-04	6.87E+01	Ac	228	890228	2.21E+04
0.5725102	3.15E-04	6.88E+01	Ac	228	890228	2.21E+04
0.5804264	1.34E-06	2.93E-01	Bi	212	830212	3.63E+03
0.5815247	2.55E-03	5.56E+02	Ac	228	890228	2.21E+04
0.5830215	5.22E-02	1.14E+04	Tl	208	810208	1.83E+02
0.5832753	2.55E-04	5.58E+01	Ac	228	890228	2.21E+04
0.5878165	2.43E-05	5.31E+00	Tl	208	810208	1.83E+02
0.6158547	1.47E-04	3.22E+01	Ac	228	890228	2.21E+04
0.6198847	1.81E-04	3.96E+01	Ac	228	890228	2.21E+04
0.6202721	6.09E-06	1.33E+00	Bi	212	830212	3.63E+03
0.6235925	1.12E-04	2.45E+01	Ac	228	890228	2.21E+04
0.6299263	8.47E-05	1.85E+01	Ac	228	890228	2.21E+04
0.6406739	1.03E-04	2.25E+01	Ac	228	890228	2.21E+04
0.6491867	7.37E-05	1.61E+01	Ac	228	890228	2.21E+04
0.6500542	1.19E-05	2.59E+00	Ra	224	880224	3.16E+05
0.6501351	2.19E-05	4.78E+00	Tl	208	810208	1.83E+02
0.651439	1.72E-04	3.76E+01	Ac	228	890228	2.21E+04
0.6604305	2.21E-05	4.83E+00	Ac	228	890228	2.21E+04
0.6663728	7.86E-05	1.72E+01	Ac	228	890228	2.21E+04
0.673864	1.72E-04	3.76E+01	Ac	228	890228	2.21E+04
0.6770728	1.45E-03	3.16E+02	Ac	228	890228	2.21E+04
0.6875821	6.39E-05	1.39E+01	Ac	228	890228	2.21E+04
0.6880483	6.39E-05	1.39E+01	Ac	228	890228	2.21E+04
0.6925034	5.78E-06	1.26E+00	Ac	228	890228	2.21E+04
0.7017969	3.29E-04	7.19E+01	Ac	228	890228	2.21E+04
0.7052351	1.34E-05	2.92E+00	Tl	208	810208	1.83E+02
0.7074949	2.59E-04	5.66E+01	Ac	228	890228	2.21E+04
0.7219105	1.23E-04	2.69E+01	Tl	208	810208	1.83E+02
0.7266278	1.47E-03	3.22E+02	Ac	228	890228	2.21E+04
0.7272466	1.13E-02	2.46E+03	Bi	212	830212	3.63E+03
0.7376714	6.88E-05	1.50E+01	Ac	228	890228	2.21E+04
0.7392292	4.82E-06	1.05E+00	Ac	228	890228	2.21E+04
0.7443224	7.76E-06	1.70E+00	Ac	228	890228	2.21E+04
0.7485842	2.61E-05	5.71E+00	Tl	208	810208	1.83E+02
0.7552773	2.24E-03	4.88E+02	Ac	228	890228	2.21E+04
0.7625131	1.16E-09	2.52E-04	Fr	224	870224	1.60E+02

0.7630576	9.97E-04	2.18E+02	Tl	208	810208	1.83E+02
0.7722775	1.85E-03	4.03E+02	Ac	228	890228	2.21E+04
0.773963	1.47E-04	3.22E+01	Ac	228	890228	2.21E+04
0.7821229	9.97E-04	2.18E+02	Ac	228	890228	2.21E+04
0.7855095	1.88E-03	4.10E+02	Bi	212	830212	3.63E+03
0.7910482	3.49E-05	7.63E+00	Ac	228	890228	2.21E+04
0.7911517	4.91E-05	1.07E+01	Ac	228	890228	2.21E+04
0.7947914	7.77E-03	1.70E+03	Ac	228	890228	2.21E+04
0.801829	5.50E-10	1.20E-04	Fr	224	870224	1.60E+02
0.8166165	5.93E-05	1.30E+01	Ac	228	890228	2.21E+04
0.8211387	2.43E-05	5.31E+00	Tl	208	810208	1.83E+02
0.8252602	9.82E-05	2.15E+01	Ac	228	890228	2.21E+04
0.8305857	1.07E-03	2.34E+02	Ac	228	890228	2.21E+04
0.8316205	1.58E-10	3.46E-05	Fr	224	870224	1.60E+02
0.8356032	2.90E-03	6.33E+02	Ac	228	890228	2.21E+04
0.8367613	5.40E-09	1.18E-03	Fr	224	870224	1.60E+02
0.8404411	1.59E-03	3.47E+02	Ac	228	890228	2.21E+04
0.8535999	2.44E-05	5.34E+00	Ac	228	890228	2.21E+04
0.8603036	7.29E-03	1.59E+03	Tl	208	810208	1.83E+02
0.8704656	1.12E-04	2.45E+01	Ac	228	890228	2.21E+04
0.8739196	3.26E-10	7.12E-05	Fr	224	870224	1.60E+02
0.87443	1.42E-04	3.11E+01	Ac	228	890228	2.21E+04
0.8776516	3.44E-05	7.51E+00	Ac	228	890228	2.21E+04
0.8810068	4.66E-10	1.02E-04	Fr	224	870224	1.60E+02
0.8832692	1.88E-05	4.11E+00	Tl	208	810208	1.83E+02
0.8839855	1.72E-04	3.76E+01	Ac	228	890228	2.21E+04
0.8874606	3.44E-05	7.51E+00	Ac	228	890228	2.21E+04
0.8934199	6.21E-04	1.36E+02	Bi	212	830212	3.63E+03
0.9042878	1.51E-03	3.30E+02	Ac	228	890228	2.21E+04
0.9111572	4.87E-02	1.06E+04	Ac	228	890228	2.21E+04
0.9191851	4.67E-05	1.02E+01	Ac	228	890228	2.21E+04
0.9222845	3.50E-05	7.64E+00	Ac	228	890228	2.21E+04
0.9239459	3.85E-05	8.41E+00	Ac	228	890228	2.21E+04
0.9274171	7.59E-05	1.66E+01	Tl	208	810208	1.83E+02
0.9310728	2.46E-05	5.37E+00	Ac	228	890228	2.21E+04
0.9406464	6.42E-05	1.40E+01	Ac	228	890228	2.21E+04
0.9439235	1.82E-04	3.97E+01	Ac	228	890228	2.21E+04
0.948351	2.06E-04	4.51E+01	Ac	228	890228	2.21E+04
0.9521726	2.98E-04	6.52E+01	Bi	212	830212	3.63E+03
0.9583036	5.21E-04	1.14E+02	Ac	228	890228	2.21E+04
0.9646375	9.78E-03	2.14E+03	Ac	228	890228	2.21E+04
0.9682576	4.94E-10	1.08E-04	Fr	224	870224	1.60E+02
0.9689707	2.95E-02	6.45E+03	Ac	228	890228	2.21E+04

0.9757648	2.02E-04	4.41E+01	Ac	228	890228	2.21E+04
0.9796728	3.93E-05	8.58E+00	Ac	228	890228	2.21E+04
0.9825171	1.20E-04	2.61E+01	Tl	208	810208	1.83E+02
0.9878698	5.76E-04	1.26E+02	Ac	228	890228	2.21E+04
0.98794	3.24E-04	7.08E+01	Ac	228	890228	2.21E+04
1.0161171	4.23E-05	9.25E+00	A	c 228	890228	2.21E+04
1.01965	4.23E-05	9.25E+00	A	c 228	890228	2.21E+04
1.033322	2.62E-04	5.72E+01	A	c 228	890228	2.21E+04
1.0399701	9.38E-05	2.05E+01	A	c 228	890228	2.21E+04
1.04135	5.40E-05	1.18E+01	A	c 228	890228	2.21E+04
1.0525142	2.52E-10	5.49E-05	F	r 224	870224	1.60E+02
1.0543009	5.36E-05	1.17E+01	A	c 228	890228	2.21E+04
1.0650465	2.89E-04	6.32E+01	A	c 228	890228	2.21E+04
1.0740665	2.68E-05	5.85E+00	B	i 212	830212	3.63E+03
1.0786919	9.07E-04	1.98E+02	B	i 212	830212	3.63E+03
1.0936255	2.25E-04	4.91E+01	T	l 208	810208	1.83E+02
1.0958738	2.23E-04	4.87E+01	A	c 228	890228	2.21E+04
1.1040055	2.95E-05	6.44E+00	A	c 228	890228	2.21E+04
1.1106962	6.56E-04	1.43E+02	A	c 228	890228	2.21E+04
1.1169742	1.03E-04	2.25E+01	A	c 228	890228	2.21E+04
1.1255842	3.04E-06	6.64E-01	T	l 208	810208	1.83E+02
1.1353889	2.06E-05	4.51E+00	A	c 228	890228	2.21E+04
1.1427406	1.72E-05	3.76E+00	A	c 228	890228	2.21E+04
1.1536873	2.70E-04	5.90E+01	A	c 228	890228	2.21E+04
1.1605509	6.68E-06	1.46E+00	T	l 208	810208	1.83E+02
1.1619626	4.84E-10	1.06E-04	F	r 224	870224	1.60E+02
1.1635566	1.28E-04	2.79E+01	A	c 228	890228	2.21E+04
1.1736912	8.38E-11	1.83E-05	F	r 224	870224	1.60E+02
1.1747876	4.91E-05	1.07E+01	A	c 228	890228	2.21E+04
1.1850842	1.03E-05	2.26E+00	T	l 208	810208	1.83E+02
1.1857911	1.21E-10	2.65E-05	F	r 224	870224	1.60E+02
1.2163986	4.42E-05	9.66E+00	A	c 228	890228	2.21E+04
1.2199023	9.32E-11	2.04E-05	F	r 224	870224	1.60E+02
1.2452262	1.47E-04	3.22E+01	A	c 228	890228	2.21E+04
1.2466005	9.58E-04	2.09E+02	A	c 228	890228	2.21E+04
1.2498092	9.82E-05	2.15E+01	A	c 228	890228	2.21E+04
1.2775435	3.44E-05	7.51E+00	A	c 228	890228	2.21E+04
1.2826842	3.16E-05	6.90E+00	T	l 208	810208	1.83E+02
1.2866472	2.01E-04	4.40E+01	A	c 228	890228	2.21E+04
1.2982578	4.47E-10	9.77E-05	F	r 224	870224	1.60E+02
1.3000665	1.22E-05	2.66E+00	B	i 212	830212	3.63E+03
1.3095728	3.56E-05	7.77E+00	A	c 228	890228	2.21E+04
1.3147638	3.59E-05	7.83E+00	A	c 228	890228	2.21E+04

1.3401912	2.35E-09	5.13E-04	F	r 224	870224	1.60E+02
1.3475857	2.21E-05	4.83E+00	A	c 228	890228	2.21E+04
1.3513984	5.31E-10	1.16E-04	F	r 224	870224	1.60E+02
1.3575848	4.91E-05	1.07E+01	A	c 228	890228	2.21E+04
1.3742601	3.39E-05	7.40E+00	A	c 228	890228	2.21E+04
1.3777152	1.60E-09	3.50E-04	F	r 224	870224	1.60E+02
1.3809841	4.25E-06	9.29E-01	T	l 208	810208	1.83E+02
1.415749	4.42E-05	9.66E+00	A	c 228	890228	2.21E+04
1.4309728	5.40E-05	1.18E+01	A	c 228	890228	2.21E+04
1.4356549	9.32E-10	2.04E-04	F	r 224	870224	1.60E+02
1.4512496	3.09E-05	6.76E+00	A	c 228	890228	2.21E+04
1.4591932	1.79E-03	3.92E+02	A	c 228	890228	2.21E+04
1.4687974	3.44E-05	7.51E+00	A	c 228	890228	2.21E+04
1.4811587	3.44E-05	7.51E+00	A	c 228	890228	2.21E+04
1.4960311	1.78E-03	3.89E+02	A	c 228	890228	2.21E+04
1.5014408	9.82E-04	2.15E+02	A	c 228	890228	2.21E+04
1.5038676	4.83E-05	1.05E+01	A	c 228	890228	2.21E+04
1.5127531	5.30E-04	1.16E+02	B	i 212	830212	3.63E+03
1.5288728	1.13E-04	2.47E+01	A	c 228	890228	2.21E+04
1.5373973	8.30E-05	1.81E+01	A	c 228	890228	2.21E+04
1.5485004	7.29E-05	1.59E+01	A	c 228	890228	2.21E+04
1.5569696	3.44E-04	7.51E+01	A	c 228	890228	2.21E+04
1.5676912	3.07E-10	6.72E-05	F	r 224	870224	1.60E+02
1.572031	8.45E-05	1.85E+01	A	c 228	890228	2.21E+04
1.5732716	9.33E-05	2.04E+01	A	c 228	890228	2.21E+04
1.5734912	2.33E-10	5.09E-05	F	r 224	870224	1.60E+02
1.5802836	1.20E-03	2.63E+02	A	c 228	890228	2.21E+04
1.5882271	6.08E-03	1.33E+03	A	c 228	890228	2.21E+04
1.6100178	1.96E-05	4.29E+00	A	c 228	890228	2.21E+04
1.6206632	2.56E-03	5.58E+02	B	i 212	830212	3.63E+03
1.6212802	1.68E-10	3.66E-05	F	r 224	870224	1.60E+02
1.6250651	5.40E-04	1.18E+02	A	c 228	890228	2.21E+04
1.6304746	3.30E-03	7.21E+02	A	c 228	890228	2.21E+04
1.6380969	9.19E-04	2.01E+02	A	c 228	890228	2.21E+04
1.6473842	1.22E-06	2.65E-01	T	l 208	810208	1.83E+02
1.6520912	5.59E-10	1.22E-04	F	r 224	870224	1.60E+02
1.6584912	1.21E-10	2.65E-05	F	r 224	870224	1.60E+02
1.6664313	3.37E-04	7.36E+01	A	c 228	890228	2.21E+04
1.6703911	1.21E-10	2.65E-05	F	r 224	870224	1.60E+02
1.6779069	1.13E-04	2.47E+01	A	c 228	890228	2.21E+04
1.6794156	1.16E-04	2.53E+01	B	i 212	830212	3.63E+03
1.6860034	1.77E-04	3.86E+01	A	c 228	890228	2.21E+04
1.7023054	1.13E-04	2.47E+01	A	c 228	890228	2.21E+04

1.7055365	1.49E-10	3.26E-05	F	r 224	870224	1.60E+02
1.7060654	2.31E-05	5.05E+00	A	c 228	890228	2.21E+04
1.7126237	1.49E-10	3.26E-05	F	r 224	870224	1.60E+02
1.7132513	7.93E-06	1.73E+00	A	c 228	890228	2.21E+04
1.7242445	5.40E-05	1.18E+01	A	c 228	890228	2.21E+04
1.7390516	3.29E-05	7.19E+00	A	c 228	890228	2.21E+04
1.7411727	2.60E-05	5.69E+00	A	c 228	890228	2.21E+04
1.743569	1.22E-06	2.65E-01	T	l 208	810208	1.83E+02
1.7508728	1.57E-05	3.43E+00	A	c 228	890228	2.21E+04
1.7578842	7.01E-05	1.53E+01	A	c 228	890228	2.21E+04
1.7844728	1.62E-05	3.54E+00	A	c 228	890228	2.21E+04
1.8013092	3.04E-05	6.64E+00	B	i 212	830212	3.63E+03
1.8059344	1.89E-04	4.12E+01	B	i 212	830212	3.63E+03
1.823469	8.62E-05	1.88E+01	A	c 228	890228	2.21E+04
1.8350991	6.88E-05	1.50E+01	A	c 228	890228	2.21E+04
1.842285	8.20E-05	1.79E+01	A	c 228	890228	2.21E+04
1.8711727	4.42E-05	9.66E+00	A	c 228	890228	2.21E+04
1.8869178	2.01E-04	4.38E+01	A	c 228	890228	2.21E+04
1.9000983	7.85E-06	1.71E+00	A	c 228	890228	2.21E+04
1.9074615	8.01E-05	1.75E+01	A	c 228	890228	2.21E+04
1.9302728	4.18E-05	9.12E+00	A	c 228	890228	2.21E+04
1.9525027	1.23E-04	2.68E+01	A	c 228	890228	2.21E+04
1.9652748	3.99E-05	8.72E+00	A	c 228	890228	2.21E+04
2.2000667	3.04E-05	6.65E+00	B	i 212	830212	3.63E+03
2.6143542	6.08E-02	1.33E+04	T	l 208	810208	1.83E+02